The Case for Phytoplankton Blooms Under Antarctic Sea Ice

Christopher Horvat[1,1,1], Sarah Seabrook[2,2,2], Antonia Cristi[2,2,2], Lisa Matthes[3,3,3], and Kelsey M Bisson[4,4,4]

[1]Brown University
[2]National Institute of Water and Atmospheric Research
[3]University of Manitoba
[4]Oregon State University

November 30, 2022

Abstract

Areas covered in compact sea ice are often assumed to prohibit upper ocean photosynthesis. Yet under-ice phytoplankton blooms (UIBs) have increasingly been observed in the Arctic, driven by anthropogenic changes to the optical properties of Arctic sea ice. Here we show the Southern Ocean can also support widespread UIBs. Using under ice-enabled BGC-Argo float data, we detail numerous high phytoplankton biomass events below compact sea ice preceding seasonal ice retreat, and classify 12 distinct UIB events. Using joint light, sea ice, and ocean conditions obtained from the ICESat-2 laser altimeter and 11 climate model contributions to CMIP6, we find that more than 4 million square kilometers of the compact-ice-covered Southern Ocean could support these events in late spring and early summer.

Phytoplankton Blooms Under Antarctic Sea Ice

Christopher Horvat,[1*], Kelsey Bisson[2], Sarah Seabrook,[3,4], Antonia Cristi, [3,5]
Lisa Matthes[6]

[1]Institute at Brown for Environment and Society, Brown University, Providence, RI, USA
[2]Department of Botany and Plant Pathology, Oregon State University, Corvallis, OR, USA
[3]National Institute of Water and Atmospheric Research, Wellington, NZ
[4]School of the Environment, University of Auckland, Auckland, NZ
[5]Department of Marine Sciences, University of Otago, Dunedin, NZ
[6]Takuvik Joint International Laboratory, Université Laval, Quebec City, QC, CA

*To whom correspondence should be addressed; E-mail: horvat@brown.edu.

Areas covered in compact sea ice are often assumed to prohibit upper ocean photosynthesis. Yet under-ice phytoplankton blooms (UIBs) have increasingly been observed in the Arctic, driven by anthropogenic changes to the optical properties of Arctic sea ice. Here we show the Southern Ocean can also support widespread UIBs. Using under ice-enabled BGC-Argo float data, we detail numerous high phytoplankton biomass events below compact sea ice preceding seasonal ice retreat, and classify 12 distinct UIB events. Using joint light, sea ice, and ocean conditions obtained from the ICESat-2 laser altimeter and 11 climate model contributions to CMIP6, we find that more than 4 million square kilometers of the compact-ice-covered Southern Ocean could support these events in late spring and early summer.

1 Introduction

Observations of under-ice phytoplankton blooms (UIBs) in the Arctic Ocean [1] have highlighted the need to understand ecological communities living under compact (local concentration greater than 80%) sea ice, now and under future climate change scenarios [2, and references within]. Regions supporting UIBs in the Arctic have likely expanded as sea ice has thinned and become more seasonal. Yet to date, no studies have described nor quantified the potential for widespread UIBs under Antarctic sea ice, where annual and seasonal variability has changed less than in the Arctic over the satellite period [3] and where sea ice is typically thinner, more seasonal, and more fragmented.

Antarctic sea ice typically has a higher albedo than Arctic sea ice [4, 5]. Thus a limited amount of photosynthetically available radiation (PAR, 400-700 nm) can reach the upper ocean directly through sea ice, especially compared to the Arctic, where light transmission through melt-pond-covered sea ice is thought to be a primary cause of UIBs [6]. Still, spring-summer solar irradiance is high: recently a bloom of nanoflagellates was observed under highly reflective landfast sea ice [7]. Floating sea ice in the Southern Ocean is also fractured, thin, and mobile. Small areas of open water, like leads or small openings within the floe mosaic, can allow substantial amounts of light to reach the upper ocean. Sunlight entering the ocean through leads in the Arctic has been shown to initiate phytoplankton blooms, even in areas where sea ice is thick and snow-covered [8]. We therefore investigate this possibility across the sea-ice-covered Southern Ocean.

Phytoplankton communities in the Southern Ocean respond rapidly to changes in light conditions, with phytoplankton blooms often observed as soon as the sea ice edge retreats in spring, flooding the mixed layer with light and leaving freshwater rich in iron, main limiters of primary production [9, 10, 11]. In the Arctic, a crucial factor in the development of UIBs is a stable

surface mixed layer, which can be induced by melt water and/or increased solar heating of the surface layer [12, 13]. Observations using tagged seals in the Ross Sea show the initiation of a shallow (20 m) surface mixed layer driven by ice melt, preceding the seasonal retreat of sea ice [14]. Yet while shallow mixed layer depths may be necessary to keep phytoplankton in the well-lit surface layer, observations from under-ice Argo floats [15, 16] demonstrate that primary production can be initiated before seasonal sea ice retreat, and even before the restratification of surface waters. This challenges the notion that too-deep surface mixed layers in ice-covered regions of the Southern Ocean limit productivity. Together these factors present the possibility that non-coastal regions of the Southern Ocean, much like the Arctic, are productive before sea ice retreats in summer.

Here we assess the potential for widespread phytoplankton growth under compact, floating, sea ice in the Southern Ocean. Our primary lines of evidence for observing UIBs are particulate-backscatter-derived phytoplankton carbon (PC) and fluorometric Chlorophyll-a (Chl-a) derived from under-ice biogeochemical Argo float data (BGC-Argo) (see methods), and we report both Chl_{max}, the maximum Chl-a recorded in each profile, and PC values at the depth of Chl_{max} (PC_{max}). While Chl-a is a pigment common to all phytoplankton and has historically been favored as a metric for phytoplankton, including in under ice studies [17, 18], attributing all changes in Chl-a to biomass may be biased because of mechanistic (i.e., photoacclimation, nutrient conditions, growth stage) and methodological concerns [19, 20, 21]. Thus we use Chl-a in conjunction with nitrate and dissolved oxygen, as data to validate and contextualize observations of enhanced PC.

After quality control, we examine 38 BGC-Argo floats that operated under sea ice in the Southern Ocean over the period from 2014-2020. 29 could have recorded UIBs as they returned profiles under compact sea ice in austral spring-summer. Nearly all such floats (24/29) record enhanced levels of phytoplankton carbon under compact ice, and 11 record UIBs. These 11

account for nearly half (196/403) of profiles examined for UIBs.

Using supporting Argo, PAR, and sea ice data, we show that UIB measurements follow representative dynamics for light-limited blooms, and use this to define a series of simple criteria for under-ice photosynthetic activity which is applied to data from ICESat-2 laser altimetry and 11 climate model assessments of Southern Ocean sea ice, light and ocean conditions. Supporting BGC-Argo data, we find the conditions required for such light-limited phytoplankton blooms are predicted across nearly 50% of regions with compact ice in spring and summer.

These results suggest that in compact, but not completely ice-covered regions of the Southern Ocean, enough light reaches into the upper water column to permit primary production, as found in the Arctic [8]. We identify potential sampling regions for examining under-ice primary production and community composition in the Ross Sea, and discuss the implications for sampling strategies and cruise timing.

2 Observations of phytoplankton blooms under compact sea ice

Biogeochemical Argo floats record many instances of high phytoplankton biomass under compact sea ice in spring-summer. In Fig. 1(a) we scatter maximum Chl-a measurements for BGC-Argo profiles (Chl_{max}, units mg/m^3 see methods) for the months of September to December when local sea ice concentration (SIC) exceeds 80%, overlaid on September-November climatological SIC. For consistency with previous BGC-Argo work [22], and to support Chl_{max} observations, we compare Chl_{max} measurements with particulate backscattering data (b_{bp}, at 700nm, units m^{-1}) taken at the depth of maximum Chl-a, which we use to compute phytoplankton carbon PC_{max} (units mg/m^3, see methods). We found comparable seasonal cycles under compact ice and a high association (Spearman's R=0.7) between the two (see Supporting Information, Fig. S2). Example profiles of Chl-a and b_{bp} are provided as Supporting Figure S4

with Chl_{max} varying from 0.1 to 3.5 mg/m^3, showing typical covariance of b_{bp} with Chl-a.

We considered 38 BGC-Argo floats that operated under sea ice in the Southern Ocean, in total recording 1117 profiles. 34 of these floats recorded 873 profiles under compact sea ice, 32 floats recorded 522 profiles during the period from September-December, leaving 29 that recorded 403 profiles under compact sea ice in this period. We define two thresholds to characterize under-ice phytoplankton biomass, based on Chl-a and PC measurements. First we define profiles where both PC_{max} and Chl_{max} exceed the interquartile range (of all 1117 profiles) of 13.3 mg/m^3 and 0.13 mg/m^3, respectively, as having "elevated" photosynthetic activity. 24 out of 29 floats under compact ice from September-December recorded such profiles. The six floats that did not observe elevated PC_{max} and Chl_{max} accounted for just 28 total profiles under compact sea ice.

We further define "UIBs" when September-December profiles under compact sea ice record both PC_{max} and Chl_{max} three inter-quartile ranges above the all-profile median, or 22.8 mg/m^3 and 0.36 mg/m^3, respectively. Such Chl-a values are similar to those used to characterize UIBs in the seasonally ice-covered Arctic [23, 24, 25], and the PC_{max} threshold chosen here exceeds the majority of global phytoplankton carbon observations [26]. In total, 11 of 30 floats recorded at least one UIB, and we record 23 UIB profiles across 12 distinct locations and time periods. Note here we define blooms only in a relative sense, as compared to background values measured in the Southern Ocean (i.e, not relative to the global phytoplankton carbon measurements) [19, 27], however these are not globally small values. UIB profiles record an average PC_{max} of 36.5 mg/m^3 and average Chl_{max} of 1.2 mg/m^3. For comparison, phytoplankton carbon calculated from BGC-Argo b_{bp} in the same manner ranges from 40-90 mg/m^3 during the spring North Atlantic bloom [28], and the highest PC_{max} observed here in September-December measurements is 55.0 mg/m^3. Chl-a, a photophysiological expression of adjustments to light throughout the water column, has greater uncertainty than PC_{max} for both mechanistic and observational

reasons [21], and so we use it only qualitatively to describe phytoplankton, following [17].

Of all under-ice profiles, many of the highest PC_{max} values were recorded under compact sea ice, though higher PC_{max} values were observed on average areas with a looser sea ice cover. Considering the 522 under-ice profiles taken between the months of September-December, we show box plots of PC_{max} in Figure 1(b), grouped by sea ice concentration (SIC, in 20% bin intervals) to illustrate this fact. A total of 43 profiles under sea ice recorded PC_{max} above 22.8 mg/m^3: 5 for SIC from 20%-40%, 5 for SIC from 40% to 60%, 10 for SIC from 60% to 80%, and 23 for SIC from 80% to 100% (compact ice). Median PC_{max} values are below 12.5 mg/m^3 in each SIC category, and lowest for SIC from 80-100% (9.81 mg/m^3).

The seasonal cycle in median PC_{max} increases with the seasonal cycle of downwelling solar irradiance, though most recorded UIBs occur in November, before the seasonal maximum irradiance. Box plots of PC_{max} in each month are given in Figure 1(c) for the 903 total profiles under compact sea ice. Median PC_{max} under compact ice ranged from 9.4 mg/m^3 (n=156) in August, to a high of 17.1 mg/m^3 in December (n=24). The number of recorded UIBs was 0 of 553 profiles from July-September, 3 out of 140 profiles in October, 15 out of 95 profiles in November, and 5 out of 24 profiles in December. UIB measurements were recorded under an average SIC of 94%. Because BGC-Argo float records can span multiple years, the "bloom" measurements were recorded in 12 distinct times and locations. In 7 instances, at least 2 successive profiles (Argo dives are spaced 10 days apart) were classified as UIBs, 6 including profiles taken in November, with the other including October profiles alone.

To examine the drivers of high biomass events under compact sea ice, and permit an analysis of their potential extent using climate model and observational data, we also consider the composite behavior of supplementary measurements for these profiles. In Fig. 2(a), we plot estimated surface, 25-meter average, and mixed-layer average PAR values (see methods) for each of the 12 distinct recorded UIBs, referenced in time to the first dive that recorded PC_{max} above

22.8 mg/m^3. While there is high variability in estimated surface PAR values for individual floats (grey lines), averaged across all floats, there is a noted increase in PAR towards the UIB observation. By the time of the UIB measurement, both mixed-layer average PAR and 25-meter average PAR cross a threshold of 10 μmol photons /m^2/s, which we use in Sec3 to evaluate the likelihood of observing blooms in model data. The median irradiance at this depth for all UIB measurements is 2.0 μmol photons /m^2/s, similar to observed compensation irradiance in Arctic waters [29,] and within the range of reported values in the North Atlantic [30,].

The UIBs found here have an observational signature consistent with light-limited under-ice blooms. In Fig. 2(b-d) we plot dissolved oxygen (b) and nitrate (c) at the depth of Chl$_{max}$, and (d) mixed layer depth, all as grey lines, with the average across different UIB measurements as a solid black line and the standard deviation denoted as dashed lines. Leading up to UIB measurements we note decreasing nitrate concentration, increasing dissolved oxygen, and rapidly declining mixed layer depths, covariant with increases in PAR prior to the first UIB profile. Light-limited blooms are often associated with shoaling mixed layers which keep phytoplankton in the euphotic layer [31,]. The autotrophy rate is set by light and nutrient status, and decreasing nitrate concentrations in the surface compared to deeper in the water column evince photosynthetic activity (noting that nitrate concentrations from deep mixing in the Southern Ocean would give surface values 35 umol/kg, prior to biological uptake). Autotrophy will initially exceed heterotrophy in the water column, also leading to increases in dissolved oxygen at the surface. Note that oxygen concentrations are also a function of atmospheric exchange and increased solubility of oxygen with colder waters [32,], which we do not consider here. These results may be compatible with the "disturbance-recovery" hypothesis [33, 15,], as phytoplankton are initially in deep MLD, which might act to dilute them from predators where they may accumulate prior to receiving enhanced light with shoaling MLDs. Because of the poor temporal adjacency of float observations, however, we cannot assess phytoplankton accumulation

rates needed to test that hypothesis.

3 The prevalence of blooms under Antarctic sea ice

The presented BGC-Argo float data showed numerous elevated phytoplankton carbon events under compact sea ice in the Southern Ocean, and we found 12 distinct instances which we classify as under-ice blooms, recorded under sea ice with an average SIC of 94%. Many of these UIBs were recorded in November, when Antarctic sea ice is near its seasonal maximum extent. We next quantify if conditions that support UIBs are widespread across the sea-ice covered Southern Ocean before sea ice retreat.

In Figure 3(a), we show ICESat-2-(IS2)-derived average ocean surface PAR values in the Southern Ocean in November, in which we make the simplifying assumption that no PAR reaches the upper ocean directly through sea ice (see methods). A solid line outlines the compact sea ice zone (CIZ, SIC $> 80\%$) defined using the NSIDC-CDR SIC product [34]. We also plot the 15% SIC contour, marking the edge of total sea ice extent (SIE). Regions lying inside the SIE contour but outside the CIZ are defined as marginal ice zones (MIZs), which due to the lower albedo of open water, receive higher PAR in the surface water layer compared to the CIZ. Figure 3(b) shows pre-industrial November PAR values for the CESM2 climate model (see methods), with CIZ and MIZ defined from the CESM2 model climatology. Both IS-2 and CESM2 show large areas within the CIZ where ocean surface PAR estimates exceed a "bloom" threshod of 23 μmol photons/m^2/s, sufficient for average insolation within the top 25 meters to exceed 10 μmol photons/m^2/s (see above, methods), representative of the mixed-layer PAR conditions found in BGC-Argo UIBs (Fig. 2a). For the IS-2 estimate of ocean surface PAR, 6.9 million km^2 of the November CIZ exceeds that PAR threshold, versus 5.9 million km^2 for CESM2. Because we do not have coincident ocean and sea ice melt observations at the scale of IS2 observations, IS2 estimates only indicate the presence of light in the upper ocean and may

overestimate the area that permits an UIB.

We next consider how frequently an individual grid cell would permit an UIB (see methods), a metric we term the UIB%. A spatial map of UIB% in November months is given in Figure 3(c) for CESM2. Areas within the climatological November CIZ (solid line), which has an area of 8.3 million km^2, permit an UIB 46.4% of the time. Because of year-to-year variability of the CIZ contour, areas outside of the climatological CIZ also have non-zero UIB%. In those areas, average UIB% is 19.3%.

We accumulate climatological statistics of UIB-permitting regions in Figure 3(d), comparing the climatological extent of compact sea ice (red) to the extent of UIB-permitting regions (blue). Large areas support UIBs, peaking at 5.9 million km^2 of compact ice-covered regions in November. The fraction of the CIZ that permits an UIB, the UIB fraction (UIBF), is examined in Figure 3(d) (black line, right axis), which peaks in November at an UIBF of 77%. By point of comparison, we reproduce Figure 3(d) as Figure 3(e) for the Arctic Ocean. Up to 4.3 million km^2 of the pre-industrial Arctic CIZ is permissive to UIBs, repeating the finding in [2], that large regions of the pre-industrial Arctic also supported UIBs. The seasonal maximum of Arctic UIB area occurs in June, at the peak of the solar cycle, with a peak UIBF of 52% in July. Generally, in the CESM2 picontrol experiments, we find that UIB-permitting regions in the Antarctic are (1) larger, (2) constitute a larger percentage of the CIZ, and (3) peak earlier in the annual solar cycle (November in the Antarctic versus June in the Arctic) than in the Arctic.

Southern ocean UIB statistics across CMIP6 models

In Figure 4(a,b), we plot the climatological seasonal cycle of Southern Ocean UIB area (a) and UIBF (b) for the 11 CMIP6 models (listed in Supporting Table S2). Across these models, we find a similar seasonal cycle. None of the CMIP6 models have large UIB areas before October, but 10 of 11 have a maximum UIB area in November. Only the MRI-ESM2 model shows a

maximum UIB area in December. Each has a climatological UIB area exceeding 2.66 million km^2, with a median of 4.75 million km^2. In Figure 4(c), we show box plots of annual maximum UIB area in the Antarctic for each of the models (filled), compared to annual maximum UIB area in the Arctic (unfilled) for the same years. Out of 11 models, 8 have median Antarctic UIB areas that exceed Arctic UIB areas.

We repeat Figure 4(a,c) in Figure 4(b,d) for the UIBF, with Figure 4(d) showing UIBF values during the month where UIB area is at its maximum (November or December in the Antarctic, June or July in the Arctic). Seasonal cycles of UIBF are similar between models, with most models peaking in December as the CIZ reduces in extent and ocean surface PAR increases. In 10 of 11 models, a higher fraction of the Antarctic CIZ permits an UIB than of the Arctic CIZ. Average values of UIBF range from 27-86% (average 57%) in the Antarctic, compared to 26-66% in the Arctic (average 37%). Each of the three models in which Antarctic UIB areas were less than Arctic UIB areas have higher UIBF in the Antarctic. Thus we suggest that the reason for differences in the overall magnitude of Antarctic UIB areas is due to differences in model representations of Antarctic and Arctic sea ice, not disagreements about whether sufficient PAR is available under the compact sea ice there.

4 The potential for observing UIBs in situ

Using BGC-Argo float data, we have demonstrated that high phytoplankton biomass events exist under compact sea ice in the Southern Hemisphere, preceding the seasonal loss of sea ice by several months as well as the seasonal maximum downwelling solar irradiance. Examining a series of climate model estimates of upper ocean light and sea ice conditions, we found that under-ice phytoplankton growth is permitted across wide swaths of the compact ice-covered Southern Ocean. We also found that areas permitting UIBs make up a larger percentage of compact sea ice zones in the Southern Ocean than the Arctic, with an earlier peak in the seasonal

cycle. To validate these results further, observational campaigns will be needed. We specifically focus on the potential of the Ross Sea region (see methods) to support such an event, as it is seasonally ice free, is among the highest-productivity regions of the Southern Ocean, and is known for supporting large ice-algal communities [35, 36].

In Figure 5, we plot UIB% for each of the 11 models during the model period with highest Ross Sea UIB area, which is November in 7 models and December in 4 models. All models have high UIB% in the coastal region near Cape Adare in the Western Ross Sea, which has compact sea ice into January. We identify a region at 72°S, 178.5°E with a blue square in Figure 5. A box plot of UIB% in this location for these 11 models is given in Figure 5 (bottom right), showing a median UIB% there of 62% with a minimum of 40%. Across the CMIP6 models, a mean area of 0.55 million km^2 of the Ross Sea is expected to permit UIBs, although the borders of UIB-permitting areas vary by model, and range from 0.29 million km^2 (MRI-ESM2, 49% of the Ross CIZ) to 0.95 million km^2 (NorESM2-LM, 65% of the Ross CIZ), with inter-annual variability. Independent of modeled sea-ice area coverage, a large fraction of the Ross CIZ permits UIBs in each year in all models. Figure 4 is repeated as Supporting Figure S1 for the Ross Sea region, showing that during the month of highest Ross Sea UIB area, at least 49% of the Ross CIZ permits UIBs in each model, on average 60%.

5 Discussion

Here we explored the potential for under-ice phytoplankton blooms beneath compact sea ice in the Southern Ocean using model simulations, altimetric measurements of sea ice coverage, and BCG-Argo data. We show that on 12 distinct occasions from October-December, BCG-Argo floats recorded UIBs with average maximum Chl-a measurements of 1.8 mg/m^3, and derived phytoplankton carbon at the depth of the Chl-a max of 38.0 mg/m^3, in areas with an average sea ice concentration of 93%. In addition to these direct high carbon measurements, findings of

elevated ($PC_{max} > 10$ mg/m^3, $Chl_{max} > 0.12$ mg/m^3) phytoplankton biomass in a large fraction of analyzed float data demonstrates the likelihood for primary production and blooms beneath Antarctic sea ice predating seasonal sea ice retreat. These elevated levels of PC_{max} under compact ice suggest that even for areas with low open water fraction, incident solar radiation is high enough to promote photosynthetic activity. This is similar to findings in the Arctic where small lead features were sufficient to support under-ice blooming [8], and suggests that small regions of open water are sufficient to relax light limitations on blooming in the summertime Southern Ocean. We supplemented the PC_{max} observations with observations of nitrate and oxygen taken at the depth as the Chl-a maximum and mixed-layer depths. Increasing oxygen towards the time of peak PC_{max}, together with decreasing nitrate, supplies evidence for photosynthetic activity. The high association between Chl-a and phytoplankton carbon (Spearman's R = 0.7, see Supporting Info Fig. S2), reinforces that these bio-optical events are associated with higher phytoplankton (i.e., biomass) concentration in the water column.

We further used ICESat-2 and an ensemble of climate model estimates of sea ice, light, and oceanographic conditions across the compact-ice-covered Southern Ocean to show that indeed, conditions are favorable for under-ice blooms over wide regions, with a median estimate UIB area of 4.75 million km^2 across the model ensemble. In using ICESat-2 data, we assumed no light reached through sea ice, and all light available for photosynthesis came through open water regions near compact ice. Thus these findings indicate that even in regions with local sea ice concentrations above 80%, and with no light passing directly through the ice, enough open water exists that light does not limit growth in the upper Southern Ocean [16]. As modeled and observed in the Arctic, widespread under-ice productivity, preceding the retreat of seasonal sea ice, may indicate a different ecological system under sea ice than previously understood.

The climate models considered here have inter-related sea ice and light schemes (see Supporting Table S2), and provide estimates of the light conditions in the Southern Ocean. They

may not be accurate if systematic biases in modeled Southern Ocean climate or sea ice properties exist. Still, compared against the estimate of upper ocean PAR derived from ICESat-2 data, models produce similar PAR estimates and areas of high surface light levels. We adopted a simple diagnostic criteria for when sufficient light is available to support a bloom, using a fixed PAR threshold in model data based on our observations of UIBs in BGC-Argo data, in line with Arctic modeling studies and observations of acclimation in key Antarctic phytoplankton species [37]. While some BGC-Argo floats do report PAR values, none of the ice-enabled floats used here do. Further observations and modeling of radiative transfer of PAR specifically focused on variable Antarctic sea ice (as in, for example, [38, 39]) would help constrain and evaluate PAR levels needed to trigger blooms in concert with BGC-Argo data. While the Argo data confirms that under-ice regions can be productive, because of their uneven spatial and temporal coverage (Supporting Info Fig. S3), it is not yet possible to directly compare geographic estimates of model-predicted conditions to float data, although we note that locations with the highest profile density also record more frequent UIB events. Thus here we use the Argo data in conjunction with models for understanding the possibility of under-ice blooms, but cannot directly validate model predictions of pan-Antarctic UIB extents.

The work we presented here raises an important question: if conditions beneath compact sea ice are favorable for supporting UIBs, and Antarctic sea ice coverage and downwelling irradiance has remained largely stable over the past several decades, why are there no reported observations of under-ice blooms in the Southern Ocean by underway cruises or moorings? We suggest two potential answers.

First, the detection of UIBs requires a dedicated effort to collect in situ chlorophyll data under compact sea ice. An analogy can be drawn to the Arctic Ocean, where spring-summer icebreaker research expeditions are more common. UIBs are now thought to have been widespread dating back to at least the 1950s (with an overall area coverage that has doubled since 1970 [2]).

But these phenomena, which can have some of the highest levels of integrated biomass of any ecological system [1], were rarely observed before the report of a massive under-ice bloom in the Chukchi Sea in 2011. As we show here, BGC-Argo floats permit a broader sampling of biological parameters across the Southern Hemisphere using consistent methodologies and calibrations. Mining of existing and previous under-ice Chlorophyll data, for example from the BCO-DMO archive, will be a focus of future work to understand whether such events have been observed in the past.

Second, it is possible that UIBs do not occur regularly. While nearly all BGC-Argo floats operating from September-December show elevated phytoplankton carbon measurements predating sea ice retreat, only 23 profiles, taken 11 of 30 floats operating in the right time and sea ice conditions, exceed our defined threshold for a "bloom". The threshold established here is defined in both phytoplankton carbon and Chl-a measurements - it exceeds typical values in the global oceans [26] generally and greatly exceeds typical values reported in open water and under-ice conditions in the Southern Ocean [19, 27] specifically. Of these UIB profiles, we recorded 6 events with two or more subsequent measurements meeting the "bloom" threshold. These multi-measurement events occurred in November-December 2016 (Argo id 5904767 and 5904180, which was previously discussed in [17]), October-November 2017 (Argo ids 5905100 and 5904180), and October-December 2018 (Argo ids 5905375 and 5905636). Further research into these six specific events will be necessary to rule out that the high levels of phytoplankton carbon recorded by these floats were not, for example, advected from a bloom occurring in open water. Our assessment of favorable underwater light conditions for UIBs over large areas of the compact ice zone is also based on a simple set of diagnostic criteria, not detailed biogeochemical modeling, and uses bulk estimates for light transmission and stratification. We do not take into account iron or other nutrient limitations, nor grazing pressure by higher trophic levels. Instead we follow the perspective of [11] that primary production is primarily light-limited in

summer. Thus the UIB-permitting area of the Southern Ocean estimated by CMIP6 models in this study is likely an upper bound on the areas that might bloom in a given year.

This work suggests there is potentially unexplored ecological variability beneath Southern Ocean sea ice, with several million square kilometers of the ice-covered Southern Ocean potentially permitting blooms before the seasonal retreat of the sea ice edge. We paid special attention to the frequently visited Ross Sea region, and suggest detailed measurements of physical and biogeochemical variables to study under-ice phytoplankton bloom phenology, magnitude and community composition and to compare those to known bloom dynamics in the Arctic Ocean [40]. Sampling during the sea ice-covered season will be challenging, especially as remote sensing technologies presently cannot measure chlorophyll under sea ice. Continued targeted deployment of Remotely Operated Vehicles (ROV) and other autonomous profiling floats [15, 16] to measure under-ice light availability and bio-optical parameters can be complementary to ship-based sampling, supported by ICESat-2 measurements used to remotely sense particulate backscatter in ice-free conditions [41] extended into sea-ice-covered regions.

6 Methods

Ice-enabled BGC-Argo float data Autonomous profiling Argo floats equipped with biological sensors are a foundation of Southern Ocean biogeochemical observations because they provide observations with consistent sampling methodologies in places (and at sampling frequencies) inaccessible via ships, and with depth resolution inaccessible via satellite, while experiencing minimal biofouling and lateral drift [42]. Because Argo floats drift with the currents during their transit, a portion of floats deployed in open water drift into ice-covered regions. To protect the floats from ice damage, an ice-avoidant algorithm (based on a temperature threshold) was implemented to initiate a float's descent when it encounters near freezing surface waters [43].

We calculate phytoplankton carbon from particulate backscattering data b_{bp} (700 nm) from biogeochemical Argo floats (BGC-Argo) [44]. Particulate backscattering covaries with phytoplankton biomass as phytoplankton scatter light proportional to their concentration and size [45], although b_{bp} observations do not necessarily imply the presence of only phytoplankton because b_{bp} can be elevated due to the presence of non-algal particles, especially deeper in the water column where there is enhanced particle sinking. Particulate backscatter has been shown to be a better proxy for phytoplankton carbon compared to fluorometric Chl-a ([26] with less measurement uncertainty for b_{bp} (on the order of 15%), [46] than for Argo Chl-a. We use the empirically derived phytoplankton carbon relationship in [26], after employing a standard conversion of b_{bp} (700 nm) to b_{bp} (470 nm) [47].

BGC-Argo pre-processing and quality control As in [46, 48], all float profiles of Chl-a and b_{bp} (700 nm, m^{-1}) were despiked with a 3-point moving median and we visually confirmed that peak Chl-a and phytoplankton carbon (from b_{bp}) values were not from noise in the profile. Examples of four Chl-a and b_{bp} profiles are given in Supporting Figure S4. We select phy-

toplankton carbon (PC_{max}) observations at the depth of the Chl-a maximum to confirm high backscatter measurements correspond to phytoplankton, and that high Chl-a measurements are not the result of photoacclimation.

We exclude profiles if Chl_{max} is recorded at a depth below 200 meters, or if b_{max} exceeds 0.01 m^{-1}, which is in excess of natural values of b_{bp} found in phytoplankton, possibly indicating the influence of bubbles or large particles (zooplankton) attracted to the instrumentation [49]. We also include oxygen and nitrate data (units μmol/kg) for comparison with the optical variables (see [20]). The main results of this study, namely the number of observed UIB profiles and their provenance, are insensitive to their presentation in either Chl-a measurements or phytoplankton carbon, and we remake Fig. 1 using Chl_{max} as Supporting Figure S2 to illustrate the similar seasonal cycle and number of UIBs recorded using Chl-a data alone.

We use corrected [20] and quality-controlled data distributed through SOCCOM with a quality flag of either '0' or '1,' indicating it was not checked or received a 'good' quality rating. While most of data within a profile has a flag of '0,', Chl-a has high numbers of 'bad' flags in near-surface observations compared to other variates (of all rated Chl-a observations, 67% were rated 'bad'). We masked and removed any 'bad' data prior to analysis in all cases. Parameters for the floats are sampled at 2m vertical resolution. We did not impose geographical constraints on the data other than that float data come from under ice regions in the Southern Ocean. Observations of other variates are reported at the depth of the maximum Chl-a concentration, because while the exact magnitudes of Chl-a may be uncertain, the location of maximum Chl-a in the water column is useful to explore these co-located biologically relevant variables [50, 51].

Values of PC_{max} and Chl_{max} reported here may underestimate of the true maximum phytoplankton carbon in the water column, as it is not possible to assess backscatter and Chl-a closer to the surface under sea ice because of the ice-avoidant nature of the Argo floats. Typically, ocean phytoplankton blooms are surface-intensified [1, 52]. For example, the mean depth of

Chl_{max} for the UIB profiles was 45 meters. Additionally, as we report PC_{max} as the value of phytoplankton carbon at the depth of Chl_{max}, it may not be the same as that of peak PC.

Location information for a float under sea ice is imprecise, as the latitude and longitude coordinates are calculated via a linear interpolation of the pre- and post-sea ice coordinates of a specific float. In some cases, the float will not surface in open water and post-sea ice coordinates are unavailable. Some floats lack under-ice geographic coordinates if they do not surface under open water conditions following a period under ice. Thus it is not possible to interpolate all float location while it transits an ice-covered region, and we remove such floats/dives. We excluded locations where local estimated SIC is less than 15%, profiles where b_{bp} at the depth of maximum Chl-a exceeded 0.01 m^{-1}, and profiles where a mixed layer depth could not be estimated. A list of all floats is provided in the Supporting Information Table S2.

CMIP6 model data Remote sensing technologies presently do not directly measure light or chlorophyll beneath sea ice, and most sampling strategies for Southern Ocean photosynthetic communities associated with sea ice focus on in-ice algae communities in coastal regions [53, 54, 55, 56]. We must instead turn to model estimates to describe the joint climatological light, sea ice, and ocean conditions underneath sea ice. We used an ensemble of current-generation coupled climate models contributing to the 6th Coupled Model Intercomparison Project (CMIP6).

While observations show Antarctic sea ice has been stable or increased in extent over the satellite period (1978-present), CMIP6 models consistently simulate a declining annual-average Antarctic sea-ice cover over this period [57]. Thus we did not consider it feasible to examine present-day model estimates of Antarctic sea ice state, which might incorporate biased depictions of sea ice albedo and extent. Instead we postulate that light conditions under Antarctic sea ice have remained stable over the industrial period, and use data from pre-industrial control run

simulations (CMIP6 runs titled picontrol) in this analysis. Of the full CMIP6 model dataset, 11 simulations (see Supporting Table S1) submitted the required model output we used here.

The ensemble of 11 models produced variable estimates of climate and sea ice state, despite high interrelation between their sea ice and radiative transfer model components. Different versions of the Community Sea Ice Model (CICE) are used as sea ice model components in 9 of 11 models. There are three substantively different light models, the improved [58] (B+L) δ-Eddington multiple-scattering scheme found in CICE versions 5 and above (CESM2 and NorESM2 simulations), an earlier version of the B+L scheme found in CICE version 4 (CAS), or implementations of simpler Beer-Lambert exponential attenuation of light in ice (CERFACS,MRI).

For each CMIP6 model, we defined a climatology of light and sea ice properties using the final 100 years of their respective pre-industrial spinup experiments. In Fig. 3 we specifically examined the Community Earth System Model version 2 (CESM2, [59]) model run, as it uses the more recent version of CICE and the more advanced B+L δ-Eddington light scheme. CESM2 produces an overall mean state of Antarctic sea ice that is broadly realistic compared to other CMIP6 models [57, 60], and similar output from CESM2 was analyzed to evaluate the potential for Arctic UIBs in [2].

ICESat-2 light data To supplement model estimates of light under sea ice, we approximated the light field under sea ice using the ICESat-2 laser altimeter. We utilized the L3A along-track sea ice type product (ATL07, [61]) derived from Level 2A ATL03 photon heights [62]. Sea ice types are determined using an empirical decision tree, which identifies whether a given segment is sea ice or water. We developed an estimate of SIC as the ratio of total ice segment length to total segment length. This quantity, the linear concentration c^*, is related to the SIC, which is defined over a 2-dimensional region. Given the random orientation of crack and open water

features relative to frequent satellite tracks, many repeat 1-D measurements can approximate a 2-D field when sampled sufficiently. In [63], we found global sea ice area metrics derived from passive microwave (PM) satellites were well-approximated by this method in regions where IS2 records at least 1000 individual segments per month. We adopted this same threshold in this study to define c^*. An advantage of using ICESat-2 segments instead of PM is that ICESat-2 is capable of resolving small cracks and leads that are difficult to observe in PM estimates of local SIC, particularly in summer [64, 65, 66].

From a gridded dataset of c^*, we estimated the total shortwave irradiance, I_0 ($\sim$ 300–3000 nm), reaching the upper ocean, I_0 (averaged monthly),

$$I_0 = SW(1 - c^*)(1 - \alpha_{oc}) \tag{1}$$

where $\alpha_{oc} = 0.06$ is the open water albedo and SW is the downwelling solar irradiance at the surface. This shortwave irradiance is then converted to a PAR (400-700 nm) estimate as in the CMIP6 model data (see methods below). This simple model assumes no light passes through the sea ice surface, and the only light available in ice-covered regions comes through the open water part of the area. For this reason we expect ICESat-2 derived downwelling irradiances may be conservative. For SW, we use the reanalyzed estimate of diurnal-average downwelling shortwave irradiance from [67]. We use IS2 data from January 2019-December 2020 to form the present-day climatology of I_0 that is presented in Figure 3.

Argo float sea ice concentration This study includes under-ice profiles initially obtained from 41 BGC-Argo floats suspected to be under ice based on a quality flag noting the float's position was interpolated. To obtain sea ice concentrations (SIC) in the area of float deployment, we matched geographic coordinates for each float to the daily 25-km resolution NSIDC Climate data record SIC product [34].

Argo float mixed layer depths To compute mixed layer depths, we use a density gradient method designed for Southern Ocean mixed-layer depths observed in Argo float data [68]. This method is preferred to standard threshold methods as it prevents near-surface temperature inversions associated with sea ice from impacting depth estimates. In each profile, water column density is computed from temperature and salinity observations, and the mixed layer depth is the first depth where the density gradient exceeds 0.05 kilograms /m^4. Profiles for which a mixed layer depth cannot be established are masked out as described above.

Argo PAR estimates As no under-ice BGC-Argo floats record onboard PAR estimates, we obtain an estimate of local PAR using the same formalism as with IS-2 PAR estimates 1, using the NSIDC SIC instead of IS-2-derived SIC, assuming no shortwave irradiance penetrates sea ice. Using the Argo-derived mixed layer depth H, we then define mixed-layer average PAR I_{ML} as,

$$I_{ML} = \frac{I_0}{\kappa H}\left(1 - e^{-\kappa H}\right). \tag{2}$$

Note that when referring to irradiance we refer to a diurnal average.

Criteria for permitting an UIB We define an area as "permitting" an under-ice bloom if it meets three criteria:

Compact sea ice Local sea ice concentration exceeds 80%.

An illuminated upper ocean. Average PAR in the top 25 meters of the ocean exceeds 10 μmol photons/m^2/s.

A stable or stratifying surface mixed layer. Sea ice is not refreezing and the upper ocean is non-convecting.

The UIB% is therefore defined as the percentage of model years where a grid cell meets all three criteria together. Thus the UIB% can be low if a region both if it is not frequently covered by compact sea ice, or if the light conditions and ocean stratification are not permissive of a bloom.

We focused on those ocean regions under "compact" sea ice to differentiate from phytoplankton growth known to occur as the ice edge retreats in marginal ice zones [69, 70]. Marginal ice zones are typically defined as areas where sea ice concentration is less than 80% [71, e.g.,], thus we used this cutoff to define regions that are "compact" ice.

To establish a threshold for upper-ocean PAR, we estimated average PAR, $\overline{I}$, at a depth D as,

$$\overline{I} = \frac{I_0}{\kappa D}\left[1 - \exp(-\kappa D)\right]. \tag{3}$$

Here we assumed that PAR is attenuated exponentially in water with a coefficient κ. We assumed positive photosynthesis (gains outweigh losses) occurs when the average PAR over a 25-m deep water column exceeds a threshold value of 10 μmol photons / m$^2/s$ that is exceeded by UIBs recorded in Fig. 2. This value is approximately twice the threshold of integrated daily irradiance of 4.8 μmol photons / m$^2/s$ considered to initiate a phytoplankton bloom in [72, 73, 13], and higher than the levels found to initiate growth in the Southern Ocean [15, 16].

Using $\kappa = 0.081/m$ [74] for PAR extinction in clear under-ice waters and $D = 25$ m establishes a surface PAR threshold value for blooms of $I_0^* \approx 23$ μmol photons /m^2/s. CMIP6 models typically store and output full-spectrum solar forcing to the upper ocean, but not PAR. We therefore had to convert full spectrum solar irradiance to PAR using a factor of 1.9975 μmol photons/J [75, 74].

We also included a threshold for the termination of upper-ocean convection. Under-ice blooms are unlikely to occur when active convection extends below the euphotic zone, such as when leads are actively refreezing with the ocean at its freezing point [12]. The requirement

that the upper ocean is non-convecting is similar to the "turbulent shutdown" theory used to explain mid-latitude phytoplankton blooms [76]. GCMs used here are too coarse to resolve the complex boundary layer dynamics that result from surface melting of sea ice [77, 78, 79], and thus they are not suited for determining the convective state of the upper ocean in the presence of sea ice leads. Instead, we considered the ocean to be non-convecting if sea ice was melting at its base, which would lead to stratification of the upper ocean, consistent with Argo observations of high negative covariance between shoaling MLD and phytoplankton biomass under ice [18]. In practice, simply non-zero basal melting does not restrict the location of UIBs as small monthly-averaged basal melt rates occur whenever sea ice is present. We therefore set a positive threshold for the sea ice basal melt rate $\dot{h}$, which we expressed as an equivalent heat flux $Q = \rho_i L_f \dot{h}$, with ρ_i = 920 kg/m^3 the sea ice density and $L_f = 3.34 \times 10^{-5}$ J/kg the latent heat of fusion. As a result Q is required to exceed 5 W/m^2, for an approximate basal melt rate of $\dot{h} = 5$ cm/month. While turbulent vertical mixing related to sea ice motion can have a significant impact on local circulation, it does not typically extend beyond several meters in the ocean [80, 81], and therefore likely does not impact convection at the depths of Chl$_{max}$ considered here.

The Ross Sea region To define the "Ross Sea region", we roughly followed the convention established by the NIWA Ross Sea Trophic Model [82], taking the ocean region south of 69°S and between 160°W and 170°E longitude. Because of grid variations, the area of this region can vary between CMIP6 models, but its surface area is approximately 1.5 million km^2.

References

[1] Arrigo, K. R. *et al.* Massive Phytoplankton Blooms Under Arctic Sea Ice. *Science* **336**, 1408 (2012). URL

http://www.sciencemag.org/cgi/doi/10.1126/science.1215065.
9605103.

[2] Ardyna, M. *et al.* Under-Ice Phytoplankton Blooms: Shedding Light on the "Invisible" Part of Arctic Primary Production. *Frontiers in Marine Science* **7**, 1–25 (2020). URL https://www.frontiersin.org/articles/10.3389/fmars.2020.608032/full.

[3] Parkinson, C. L. A 40-y record reveals gradual Antarctic sea ice increases followed by decreases at rates far exceeding the rates seen in the Arctic. *Proceedings of the National Academy of Sciences of the United States of America* **116**, 14414–14423 (2019).

[4] Brandt, R. E., Warren, S. G., Worby, A. P. & Grenfell, T. C. Surface Albedo of the Antarctic Sea Ice Zone. *Journal of Climate* **18**, 3606–3622 (2005). URL https://journals.ametsoc.org/jcli/article/18/17/3606/30648/Surface-Albe

[5] Arndt, S. *et al.* Influence of snow depth and surface flooding on light transmission through Antarctic pack ice. *Journal of Geophysical Research: Oceans* **122**, 2108–2119 (2017). URL http://www.nature.com/articles/175238c0
http://doi.wiley.com/10.1002/2016JC012325.

[6] Arrigo, K. R. *et al.* Phytoplankton blooms beneath the sea ice in the Chukchi sea. *Deep-Sea Research Part II: Topical Studies in Oceanography* **105**, 1–16 (2014). URL http://linkinghub.elsevier.com/retrieve/pii/S0967064514000836.

[7] Saggiomo, M., Escalera, L., Saggiomo, V., Bolinesi, F. & Mangoni, O. Phytoplankton Blooms Below the Antarctic Landfast Ice During the Melt Season Between Late Spring and Early Summer. *Journal of Phycology* **57**, 541–550 (2021). URL https://onlinelibrary.wiley.com/doi/10.1111/jpy.13112.

[8] Assmy, P. *et al.* Leads in Arctic pack ice enable early phytoplankton blooms below snow-covered sea ice. *Scientific Reports* **7**, 40850 (2017). URL http://www.nature.com/articles/srep40850.

[9] Martin, J. H., Fitzwater, S. E. & Gordon, R. M. Iron deficiency limits phytoplankton growth in Antarctic waters. *Global Biogeochemical Cycles* **4**, 5–12 (1990). URL http://doi.wiley.com/10.1029/GB004i001p00005.

[10] Comiso, J. C., McClain, C. R., Sullivan, C. W., Ryan, J. P. & Leonard, C. L. Coastal zone color scanner pigment concentrations in the Southern Ocean and relationships to geophysical surface features. *Journal of Geophysical Research: Oceans* **98**, 2419–2451 (1993). URL http://doi.wiley.com/10.1029/92JC02505.

[11] van Oijen, T. Light rather than iron controls photosynthate production and allocation in Southern Ocean phytoplankton populations during austral autumn. *Journal of Plankton Research* **26**, 885–900 (2004). URL https://academic.oup.com/plankt/article-lookup/doi/10.1093/plankt/fbh08

[12] Lowry, K. E. *et al.* Under-Ice Phytoplankton Blooms Inhibited by Spring Convective Mixing in Refreezing Leads. *Journal of Geophysical Research: Oceans* **123**, 90–109 (2018). URL http://doi.wiley.com/10.1002/2016JC012575.

[13] Oziel, L. *et al.* Environmental factors influencing the seasonal dynamics of spring algal blooms in and beneath sea ice in western Baffin Bay. *Elementa: Science of the Anthropocene* **7**, 34 (2019). URL https://online.ucpress.edu/elementa/article/doi/10.1525/elementa.372/11

[14] Porter, D. F. *et al.* Evolution of the Seasonal Surface Mixed Layer of the Ross Sea, Antarctica, Observed With Autonomous Profiling Floats. *Journal of Geophysical Research: Oceans* **124**, 4934–4953 (2019).

[15] Arteaga, L. A., Boss, E., Behrenfeld, M. J., Westberry, T. K. & Sarmiento, J. L. Seasonal modulation of phytoplankton biomass in the Southern Ocean. *Nature Communications* **11** (2020). URL http://dx.doi.org/10.1038/s41467-020-19157-2.

[16] Hague, M. & Vichi, M. Southern Ocean Biogeochemical Argo detect under-ice phytoplankton growth before sea ice retreat. *Biogeosciences* **18**, 25–38 (2021). URL https://bg.copernicus.org/articles/18/25/2021/.

[17] Briggs, E. M., Martz, T. R., Talley, L. D., Mazloff, M. R. & Johnson, K. S. Physical and Biological Drivers of Biogeochemical Tracers Within the Seasonal Sea Ice Zone of the Southern Ocean From Profiling Floats. *Journal of Geophysical Research: Oceans* **123**, 746–758 (2018). URL https://onlinelibrary.wiley.com/doi/10.1002/2017JC012846.

[18] Bisson, K. M. & Cael, B. B. How are under ice phytoplankton related to sea ice in the Southern Ocean? *Geophysical Research Letters* 1–14 (2021). URL https://onlinelibrary.wiley.com/doi/10.1029/2021GL095051.

[19] Haëntjens, N., Boss, E. & Talley, L. D. Revisiting Ocean Color algorithms for chlorophyll-a and particulate organic carbon in the Southern Ocean using biogeochemical floats. *Journal of Geophysical Research: Oceans* **122**, 6583–6593 (2017). URL https://onlinelibrary.wiley.com/doi/10.1002/2017JC012844.

[20] Johnson, K. S. *et al.* Biogeochemical sensor performance in the SOCCOM profiling float array. *Journal of Geophysical Research: Oceans* **122**, 6416–6436 (2017). URL https://onlinelibrary.wiley.com/doi/10.1002/2017JC012838.

[21] Roesler, C. *et al.* Recommendations for obtaining unbiased chlorophyll estimates from in situ chlorophyll fluorometers: A global analysis of WET Labs ECO sensors. *Limnology and Oceanography: Methods* **15**, 572–585 (2017). URL https://onlinelibrary.wiley.com/doi/10.1002/lom3.10185.

[22] Mayot, N. *et al.* Assessing Phytoplankton Activities in the Seasonal Ice Zone of the Greenland Sea Over an Annual Cycle. *Journal of Geophysical Research: Oceans* **123**, 8004–8025 (2018). URL http://doi.wiley.com/10.1029/2018JC014271.

[23] Apollonio, S. Hydrobiological measurements on IGY drifting station Bravo. *Trans. Am. Geophys. Union* **40**, 316–3 (1959).

[24] Laney, S. R. *et al.* Assessing algal biomass and bio-optical distributions in perennially ice-covered polar ocean ecosystems. *Polar Science* **8**, 73–85 (2014). URL https://linkinghub.elsevier.com/retrieve/pii/S1873965213000510.

[25] Boles, E. *et al.* Under-Ice Phytoplankton Blooms in the Central Arctic Ocean: Insights From the First Biogeochemical IAOOS Platform Drift in 2017. *Journal of Geophysical Research: Oceans* **125**, 6069–6079 (2020). URL https://onlinelibrary.wiley.com/doi/10.1029/2019JC015608.

[26] Graff, J. R. *et al.* Analytical phytoplankton carbon measurements spanning diverse ecosystems. *Deep Sea Research Part I: Oceanographic Research Papers* **102**, 16–25 (2015). URL https://linkinghub.elsevier.com/retrieve/pii/S0967063715000801.

[27] Moore, J. K. & Abbott, M. R. Phytoplankton chlorophyll distributions and primary production in the Southern Ocean. *Journal of Geophysical Research: Oceans* **105**, 28709–28722 (2000). URL http://doi.wiley.com/10.1029/1999JC000043.

[28] Cetinić, I. *et al.* Particulate organic carbon and inherent optical properties during 2008 North Atlantic bloom experiment. *Journal of Geophysical Research: Oceans* **117** (2012).

[29] Tremblay, J. É., Michel, C., Hobson, K. A., Gosselin, M. & Price, N. M. Bloom dynamics in early opening waters of the Arctic Ocean. *Limnology and Oceanography* **51**, 900–912 (2006).

[30] Siegel, D. A., Doney, S. C. & Yoder, J. A. The North Atlantic Spring Phytoplankton Bloom and Sverdrup's Critical Depth Hypothesis. *Science* **296**, 730–733 (2002). URL http://www.sciencemag.org/cgi/doi/10.1126/science.1069174.

[31] Sverdrup, H. U. On Conditions for the Vernal Blooming of Phytoplankton. *ICES Journal of Marine Science* **18**, 287–295 (1953). URL https://academic.oup.com/icesjms/article-lookup/doi/10.1093/icesjms/18.

[32] Glud, R. N., Rysgaard, S., Turner, G., McGinnis, D. F. & Leakey, R. J. G. Biological- and physical-induced oxygen dynamics in melting sea ice of the Fram Strait. *Limnology and Oceanography* **59**, 1097–1111 (2014). URL http://doi.wiley.com/10.4319/lo.2014.59.4.1097.

[33] Behrenfeld, M. J. Abandoning sverdrup's critical depth hypothesis on phytoplankton blooms. *Ecology* **91**, 977–989 (2010). URL http://www.esajournals.org/doi/abs/10.1890/09-1207.1 http://doi.wiley.com/10.1890/09-1207.1.

[34] Meier, W. N., Fetterer, F., Windnagel., A. K. & Stewart, J. S. NOAA/NSIDC Climate Data Record of Passive Microwave Sea Ice Concentration, Version 4. (2021).

[35] Lizotte, M. P. The Contributions of Sea Ice Algae to Antarctic Marine Primary Production. *American Zoologist* **41**, 57–73 (2001). URL https://academic.oup.com/icb/article-lookup/doi/10.1093/icb/41.1.57.

[36] Arrigo, K. R. Physical control of chlorophyll a , POC, and TPN distributions in the pack ice of the Ross Sea, Antarctica. *Journal of Geophysical Research* **108**, 3316 (2003). URL https://onlinelibrary.wiley.com/doi/10.1029/2001JC001138.

[37] Arrigo, K. R. *et al.* Photophysiology in two major southern ocean phytoplankton taxa: Photosynthesis and growth of phaeocystis antarctica and fragilariopsis cylindrus under different irradiance levels. *Integrative and Comparative Biology* **50**, 950–966 (2010).

[38] Horvat, C., Flocco, D., Rees Jones, D. W., Roach, L. & Golden, K. M. The Effect of Melt Pond Geometry on the Distribution of Solar Energy Under First-Year Sea Ice. *Geophysical Research Letters* **47** (2020). URL https://onlinelibrary.wiley.com/doi/abs/10.1029/2019GL085956.

[39] Katlein, C., Valcic, L., Lambert-Girard, S. & Hoppmann, M. New insights into radiative transfer within sea ice derived from autonomous optical propagation measurements. *The Cryosphere* **15**, 183–198 (2021). URL https://tc.copernicus.org/articles/15/183/2021/.

[40] Chase, A. P. *et al.* Evaluation of diagnostic pigments to estimate phytoplankton size classes. *Limnology and Oceanography: Methods* (2020).

[41] Lu, X. *et al.* Antarctic spring ice-edge blooms observed from space by ICESat-2. *Remote Sensing of Environment* **245**, 111827 (2020). URL https://doi.org/10.1016/j.rse.2020.111827.

[42] Poteau, A., Boss, E. & Claustre, H. Particulate concentration and seasonal dynamics in the mesopelagic ocean based on the backscattering coefficient measured with Biogeochemical-Argo floats. *Geophysical Research Letters* **44**, 6933–6939 (2017). URL http://doi.wiley.com/10.1002/2017GL073949.

[43] Klatt, O., Boebel, O. & Fahrbach, E. A profiling float's sense of ice. *Journal of Atmospheric and Oceanic Technology* **24**, 1301–1308 (2007). URL http://journals.ametsoc.org/doi/abs/10.1175/JTECH2026.1.

[44] Claustre, H. *et al.* Bio-Optical Profiling Floats as New Observational Tools for Biogeochemical and Ecosystem Studies: Potential Synergies with Ocean Color Remote Sensing. In *Proceedings of OceanObs'09: Sustained Ocean Observations and Information for Society*, 1, 177–183 (European Space Agency, 2010). URL http://www.oceanobs09.net/proceedings/cwp/cwp17.

[45] Hergert, W. & Wriedt, T. *The Mie theory: basics and applications* (Springer, 2012).

[46] Bisson, K. M., Boss, E., Westberry, T. K. & Behrenfeld, M. J. Evaluating satellite estimates of particulate backscatter in the global open ocean using autonomous profiling floats. *Optics Express* **27**, 30191 (2019). URL https://www.osapublishing.org/abstract.cfm?URI=oe-27-21-30191.

[47] Lee, Z., Carder, K. L. & Arnone, R. A. Deriving inherent optical properties from water color: a multiband quasi-analytical algorithm

for optically deep waters. *Applied Optics* **41**, 5755 (2002). URL https://www.osapublishing.org/abstract.cfm?URI=ao-41-27-5755.

[48] Bisson, K. M., Boss, E., Werdell, P. J., Ibrahim, A. & Behrenfeld, M. J. Particulate Backscattering in the Global Ocean: A Comparison of Independent Assessments. *Geophysical Research Letters* **48** (2021). URL https://onlinelibrary.wiley.com/doi/10.1029/2020GL090909.

[49] Haëntjens, N. *et al.* Detecting Mesopelagic Organisms Using Biogeochemical-Argo Floats. *Geophysical Research Letters* **47** (2020).

[50] Ardyna, M. *et al.* Parameterization of vertical chlorophyll a in the Arctic Ocean: Impact of the subsurface chlorophyll maximum on regional, seasonal, and annual primary production estimates. *Biogeosciences* **10**, 4383–4404 (2013).

[51] Brown, Z. W. *et al.* Characterizing the subsurface chlorophyll a maximum in the Chukchi Sea and Canada Basin. *Deep-Sea Research Part II: Topical Studies in Oceanography* **118**, 88–104 (2015). URL http://dx.doi.org/10.1016/j.dsr2.2015.02.010.

[52] SMITH, W. O. & NELSON, D. M. Phytoplankton Bloom Produced by a Receding Ice Edge in the Ross Sea: Spatial Coherence with the Density Field. *Science* **227**, 163–166 (1985). URL http://www.sciencemag.org/content/227/4683/163.shorthttp://www.sciencem

[53] Smetacek, V. *et al.* Early spring phytoplankton blooms in ice platelet layers of the southern Weddell Sea, Antarctica. *Deep Sea Research Part A. Oceanographic Research Papers* **39**, 153–168 (1992). URL https://linkinghub.elsevier.com/retrieve/pii/019801499290102Y.

706 [54] Arrigo, K. R. & Thomas, D. N. Large scale importance of sea ice biology in the Southern
707 Ocean. *Antarctic Science* **16**, 471–486 (2004).

708 [55] McMinn, A., Martin, A. & Ryan, K. Phytoplankton and sea ice al-
709 gal biomass and physiology during the transition between winter and
710 spring (McMurdo Sound, Antarctica). *Polar Biology* **33**, 1547–1556
711 (2010). URL http://www.nature.com/articles/175238c0
712 http://doi.wiley.com/10.1002/2016JC012325
713 http://link.springer.com/10.1007/s00300-010-0844-6.

714 [56] Cummings, V. J. *et al.* In situ response of Antarctic under-ice pri-
715 mary producers to experimentally altered pH. *Scientific Reports* **9**, 6069
716 (2019). URL http://dx.doi.org/10.1038/s41598-019-42329-0
717 http://www.nature.com/articles/s41598-019-42329-0.

718 [57] Roach, L. A. *et al.* Antarctic Sea Ice Area in CMIP6. *Geophysical Research Letters* 1–24
719 (2020).

720 [58] Briegleb, B. P. & Light, B. A Delta-Eddington multiple scattering parameterization for
721 solar radiation in the sea ice component of the Community Climate System Model. Tech.
722 Rep. February, National Center for Atmospheric Research (2007).

723 [59] Danabasoglu, G. *et al.* The Community Earth System Model Version 2 (CESM2). *Journal*
724 *of Advances in Modeling Earth Systems* **12**, 1–35 (2020).

725 [60] Singh, H. K. A., Landrum, L., Holland, M. M., Bailey, D. A. & DuVivier, A. K. An
726 Overview of Antarctic Sea Ice in the Community Earth System Model version 2, Part
727 I: Analysis of the Seasonal Cycle in the Context of Sea Ice Thermodynamics and Cou-

pled Atmosphere-Ocean-Ice Processes. *Journal of Advances in Modeling Earth Systems* (2020).

[61] Kwok, R. *et al.* ATLAS/ICESat-2 L3A Sea Ice Height, Version 1. Boulder, Colorado USA. Tech. Rep. May, NSIDC, Boulder, Colorado USA (2019).

[62] Neumann, T. A. *et al.* The Ice, Cloud, and Land Elevation Satellite – 2 mission: A global geolocated photon product derived from the Advanced Topographic Laser Altimeter System. *Remote Sensing of Environment* **233**, 111325 (2019). URL https://linkinghub.elsevier.com/retrieve/pii/S003442571930344X.

[63] Horvat, C., Blanchard-Wrigglesworth, E. & Petty, A. Observing waves in sea ice with ICESat-2. *Geophysical Research Letters* (2020). URL https://onlinelibrary.wiley.com/doi/abs/10.1029/2020GL087629.

[64] Kwok, R. Sea ice concentration estimates from satellite passive microwave radiometry and openings from SAR ice motion. *Geophysical Research Letters* **29**, 25–1–25–4 (2002). URL http://doi.wiley.com/10.1029/2002GL014787.

[65] Notz, D., Haumann, F. A., Haak, H., Jungclaus, J. H. & Marotzke, J. Arctic sea-ice evolution as modeled by Max Planck Institute for Meteorology's Earth system model. *Journal of Advances in Modeling Earth Systems* **5**, 173–194 (2013). URL http://dx.doi.org/10.1002/jame.20016 http://doi.wiley.com/10.1002/jame.20016.

[66] Kern, S., Lavergne, T., Notz, D., Pedersen, L. T. & Tonboe, R. Satellite passive microwave sea-ice concentration data set inter-comparison for Arctic summer conditions. *The Cryosphere* **14**, 2469–2493 (2020). URL https://tc.copernicus.org/articles/14/2469/2020/.

751 [67] Tsujino, H. *et al.* JRA-55 based surface dataset for driving ocean–sea-
752 ice models (JRA55-do). *Ocean Modelling* **130**, 79–139 (2018). URL
753 https://linkinghub.elsevier.com/retrieve/pii/S146350031830235X.

754 [68] Dong, S., Sprintall, J., Gille, S. T. & Talley, L. Southern ocean mixed-layer depth from
755 Argo float profiles. *Journal of Geophysical Research: Oceans* **113**, 1–12 (2008).

756 [69] Smith, W. O. & Nelson, D. M. Importance of Ice Edge Phytoplankton Pro-
757 duction in the Southern Ocean. *BioScience* **36**, 251–257 (1986). URL
758 https://academic.oup.com/bioscience/article-lookup/doi/10.2307/1310215.

759 [70] Perrette, M., Yool, A., Quartly, G. D. & Popova, E. E. Near-ubiquity of ice-edge blooms
760 in the Arctic. *Biogeosciences* **8**, 515–524 (2011).

761 [71] Strong, C. & Rigor, I. G. Arctic marginal ice zone trending wider in summer and
762 narrower in winter. *Geophysical Research Letters* **40**, 4864–4868 (2013). URL
763 http://doi.wiley.com/10.1002/grl.50928.

764 [72] Letelier, R. M., Karl, D. M., Abbott, M. R. & Bidigare, R. R. Light driven seasonal pat-
765 terns of chlorophyll and nitrate in the lower euphotic zone of the North Pacific Subtropical
766 Gyre. *Limnology and Oceanography* **49**, 508–519 (2004).

767 [73] Boss, E. & Behrenfeld, M. In situ evaluation of the initiation of the North Atlantic phyto-
768 plankton bloom. *Geophysical Research Letters* **37**, 1–5 (2010).

769 [74] Matthes, L. C. *et al.* Average cosine coefficient and spectral distribution of the light field
770 under sea ice: Implications for primary production. *Elementa* **7** (2019).

771 [75] Yu, X., Wu, Z., Jiang, W. & Guo, X. Predicting daily photosynthetically
772 cally active radiation from global solar radiation in the Contiguous United

States. *Energy Conversion and Management* **89**, 71–82 (2015). URL https://linkinghub.elsevier.com/retrieve/pii/S0196890414008395.

[76] Taylor, J. R. & Ferrari, R. Shutdown of turbulent convection as a new criterion for the onset of spring phytoplankton blooms. *Limnology and Oceanography* **56**, 2293–2307 (2011).

[77] Holland, M. M. An improved single-column model representation of ocean mixing associated with summertime leads: Results from a SHEBA case study. *Journal of Geophysical Research* **108**, 3107 (2003). URL http://doi.wiley.com/10.1029/2002JC001557.

[78] Horvat, C., Tziperman, E. & Campin, J.-M. Interaction of sea ice floe size, ocean eddies, and sea ice melting. *Geophysical Research Letters* **43**, 8083–8090 (2016). URL http://doi.wiley.com/10.1002/2016GL069742.

[79] Pellichero, V., Sallée, J.-B., Schmidtko, S., Roquet, F. & Charrassin, J.-B. The ocean mixed layer under Southern Ocean sea-ice: Seasonal cycle and forcing. *Journal of Geophysical Research: Oceans* **122**, 1608–1633 (2017). URL http://doi.wiley.com/10.1002/2016JC011970.

[80] Smith, M. & Thomson, J. Ocean Surface Turbulence in Newly Formed Marginal Ice Zones. *Journal of Geophysical Research: Oceans* **124**, 1382–1398 (2019). URL https://onlinelibrary.wiley.com/doi/10.1029/2018JC014405.

[81] Brenner, S., Rainville, L., Thomson, J., Cole, S. & Lee, C. Comparing Observations and Parameterizations of Ice-Ocean Drag Through an Annual Cycle Across the Beaufort Sea. *Journal of Geophysical Research: Oceans* **126** (2021).

[82] Pinkerton, M. H., Bradford-Grieve, J. M. & Hanchet, S. M. A balanced model of the food web of the Ross Sea, Antarctica. *CCAMLR Science* **17**, 1–31 (2010).

[83] Horvat, C., Seabrook, S., Cristi, A., Matthes, L. & Bisson, K. Code for: The Case for Phytoplankton Blooms Under Antarctic Sea Ice (2021).

7 Corresponding Author

All correspondence and requests for material should be addressed to Christopher Horvat, christopher_horva

8 Acknowledgements

CH was supported by NASA grant 80NSSC20K0959 and by Schmidt Futures – a philanthropic initiative that seeks to improve societal outcomes through the development of emerging science and technologies. CH thanks the National Institute of Water and Atmospheric Research in Wellington, NZ for their hospitality during parts of this work. KB was supported by NASA grant 80NSSC20K0970 and thanks Tanya Maurer at MBARI for help with Argo under ice identification. We acknowledge the World Climate Research Programme, which, through its Working Group on Coupled Modelling, coordinated and promoted CMIP6. We thank the climate modeling groups for producing and making available their model output, the Earth System Grid Federation (ESGF) for archiving the data and providing access, and the multiple funding agencies who support CMIP6 and ESGF. These Argo data were collected and made freely available by the International Argo Program and the national programs that contribute to it. (https://argo.ucsd.edu, https://www.ocean-ops.org). The Argo Program is part of the Global Ocean Observing System.

9 Author Contributions

CH and SS concieved of the study. CH performed the data analysis and prepared the manuscript. KB provided BGC-Argo data processing and analysis. All authors assisted with study design and manuscript writing.

10 Competing Interests

The authors declare no competing interests.

11 Data Availability

ICESat-2 data are available through the National Snow and Ice Data Center (NSIDC). The sea ice type product is found online at https://nsidc.org/data/ATL07/versions/3. JRA55-do and CMIP6 data used in this study are available at the Earth System Federated Grid at `https://esgf-node.lln` and `https://esgf-node.llnl.gov/projects/cmip6/`, respectively. Argo data were collected and made freely available by the Southern Ocean Carbon and Climate Observations and Modeling (SOCCOM) Project funded by the National Science Foundation, Division of Polar Programs (NSF PLR -1425989 and OPP-1936222), supplemented by NASA, and by the International Argo Program and the NOAA programs that contribute to it. `http://www.argo.ucsd.edu`, `https://soccompu.princeton.edu/www/index.html`. The Argo Program is part of the Global Ocean Observing System. Processed Argo data for making figures is included in the code repository [83].

12 Code Availability

Code for processing data and producing Antarctic under-ice light fields and UIB-permitting criteria is publicly available on github at https://github.com/chhorvat/Antarctic-Light/, with re-

leases archived in the Zenodo repository [83]. Data required to produce figures in this manuscript is included within this repository.

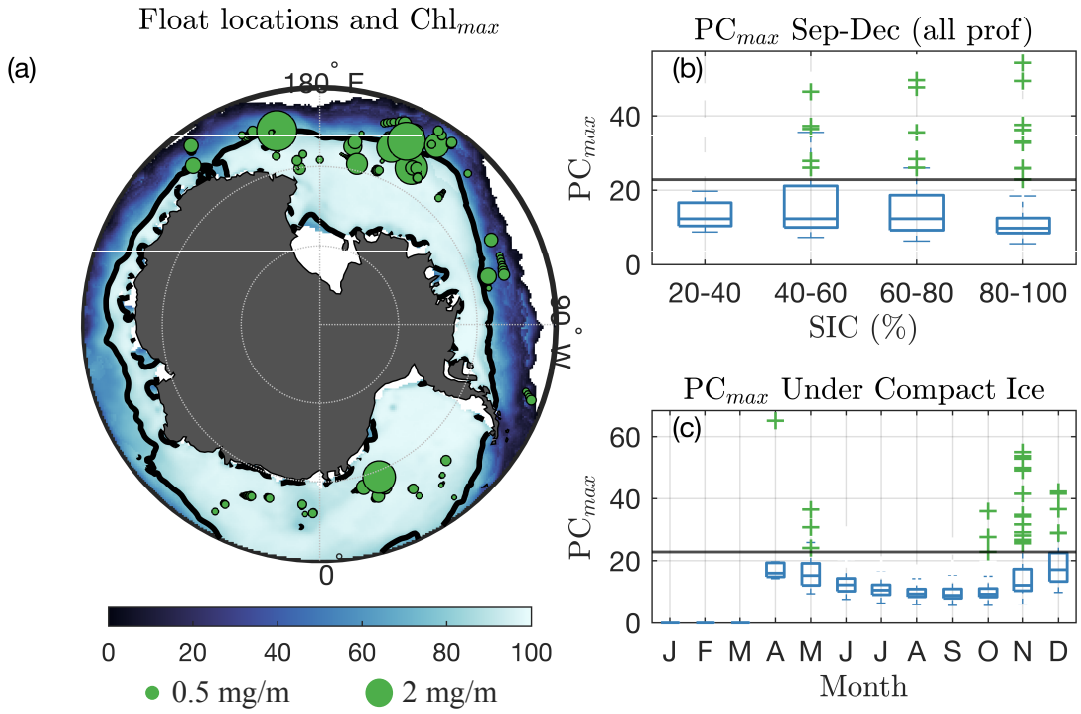

Figure 1: **Chlorophyll-a and Phytoplankton Carbon recorded under compact sea ice by BGC-Argo floats.** (a) Climatological sea ice coverage in September-November, 2014-2020. Black line shows 80% concentration contour. Green circles are locations of under-ice Argo float profiles under compact sea ice from September-December, with sizes scaled with value of Chl$_{max}$. Green dots outside of map shows sizes corresponding to 0.5 and 2.0 mg/m^3. (b) Box plot of Chl$_{max}$ for all BGC-Argo measurements under sea ice, indexed by sea ice concentration. Whiskers extend boxes ± 3 standard deviations from the mean in each month and vertical blue line is ensemble median. Crosses show values identified as UIBs. Black line is PC$_{max}$ bloom threshold. (c) Same as (b), but for PC$_{max}$ recorded under compact sea ice (concentration $>$ 80%) only, indexed by month.

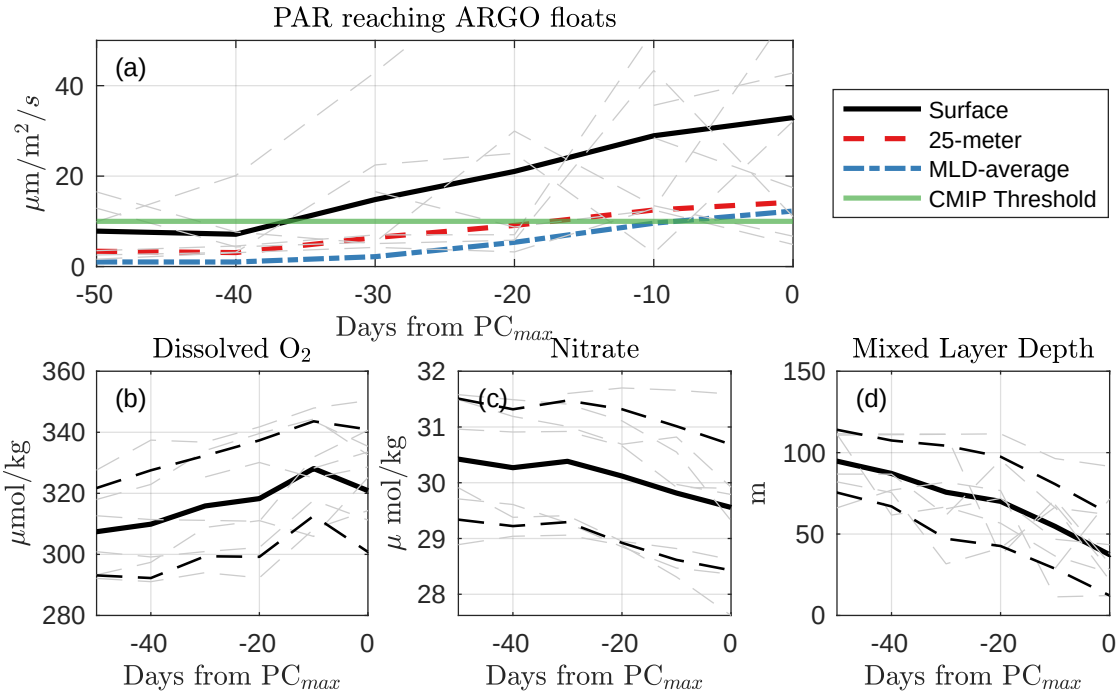

Figure 2: **Under-ice conditions preceding UIBs.** (a) averaged estimated PAR for each of the 13 measured UIBs for the first profile identified as a UIB and the 5 preceding under-ice profiles. Black line is average surface PAR. Red dash line is average PAR over top 25 meters. Blue dot-dash line is PAR averaged over Argo-measured mixed layer depth. Green line indicates the PAR threshold used to define UIBs in CMIP6 data. (b-d) Same as (a, black line) for (b) dissolved oxygen at depth of Chlorophyll-a maximum, (c) nitrate at depth of Chl$_{max}$, and (d) mixed layer depth. Dashed lines indicate standard deviation of profile measurements.

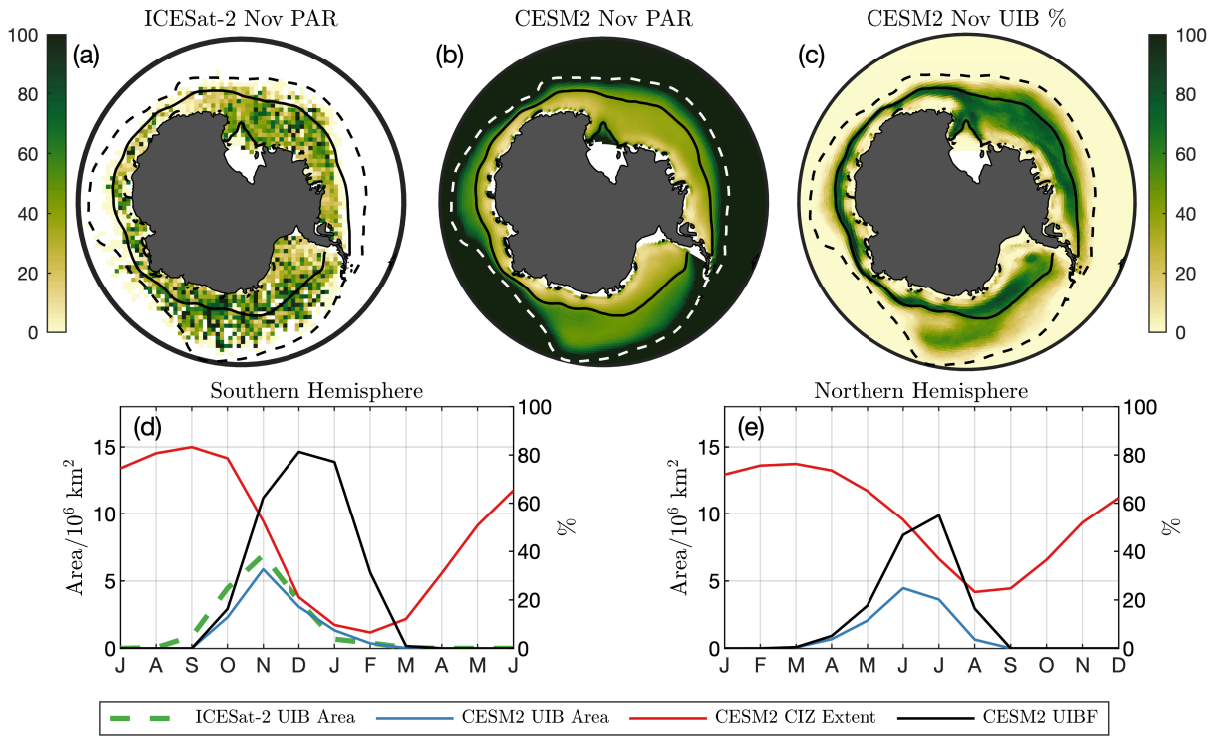

Figure 3: **Light field and UIB potential under Southern Ocean sea ice** (a) 2018-2020 November surface PAR (μmol photons/m^2/s) estimate from ICESat-2. (b) CESM2 climatological PAR from pre-industrial simulation. Solid lines in (a-b) are CESM2 climatological CIZ (concentration above 80%). Dashed lines are climatological SIE (concentration above 15%). (c) CESM2 November UIB%. (d,left axis) Seasonal cycle of CESM2 (red) CIZ extent and (blue) UIB extent. Dashed green line is UIB area from ICESat-2. (d,right axis) CESM2 UIBF. (e) As in (d), but for the Northern Hemisphere. Axes in (d) and (e) are offset by 6 months.

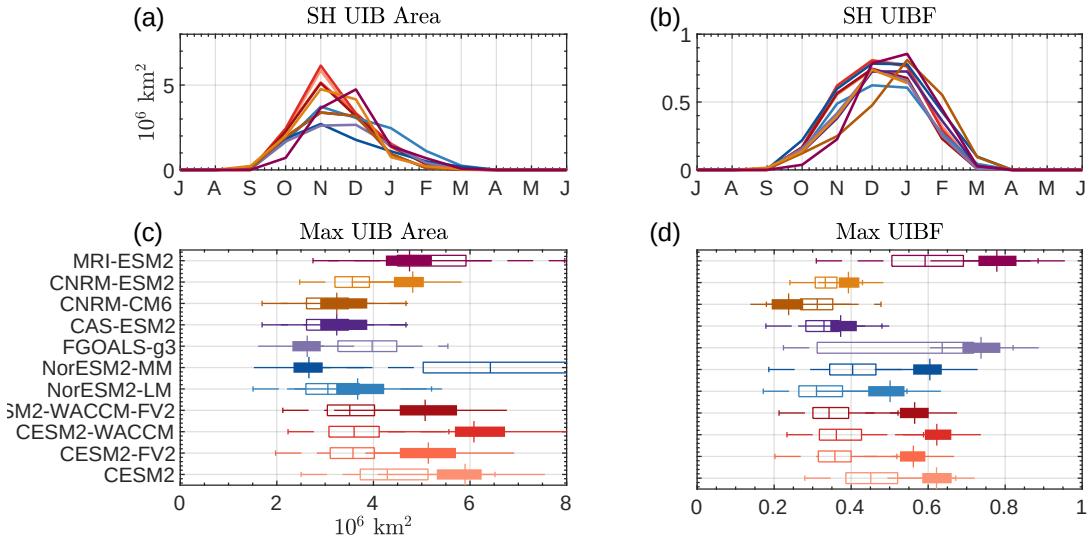

Figure 4: **Statistics of bloom-permitting area for CMIP6 models**. (a) Seasonal cycle of UIB-permitting area in the Southern Hemisphere. (b) Seasonal cycle of UIBF. (c) Box plots of maximum annual UIB area in (filled) the Southern Hemisphere or (unfilled) the Northern Hemisphere. (d) Box plots of UIBF during month of maximum UIB area. Colors of lines in (a,b) correspond to boxes in (c,d)

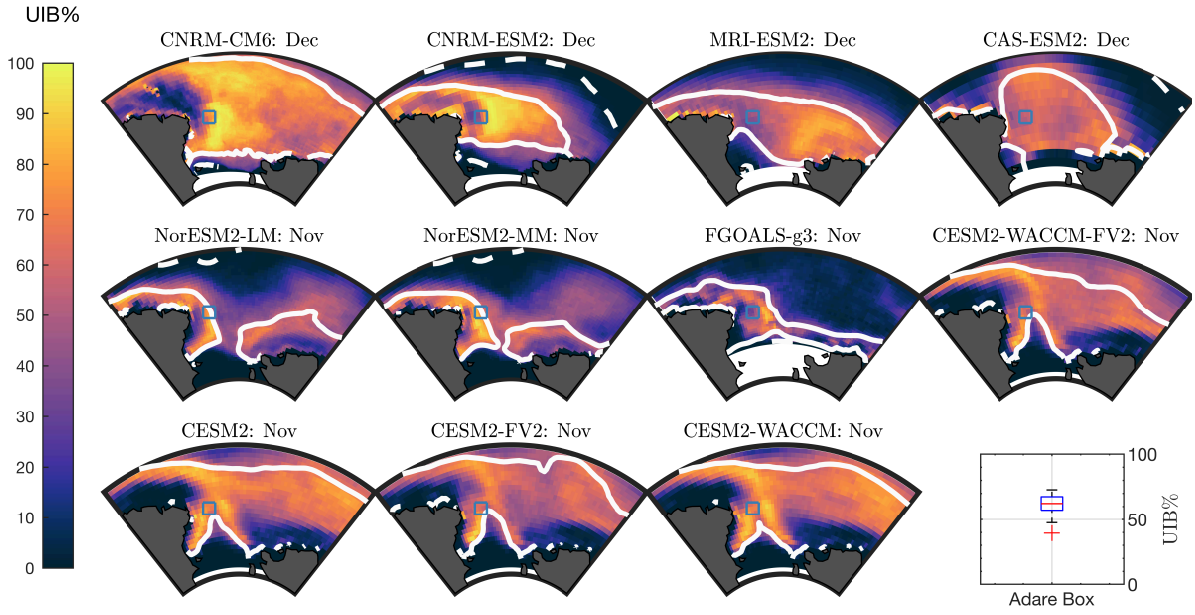

Figure 5: **UIB likelihoods in the Ross Sea.** Ross Sea UIB% for each model in the month of maximum UIB area. Solid lines are climatological CIZ. Dashed lines are climatological SIE. Blue square highlights location of interest at 72°S,178°E. Box plot (bottom right) is of UIB% at square location.

Phytoplankton Blooms Under Antarctic Sea Ice

Christopher Horvat,[1*], Kelsey Bisson[2], Sarah Seabrook,[3,4], Antonia Cristi, [3,5] Lisa Matthes,[6]

[1]Institute at Brown for Environment and Society, Brown University, Providence, RI, USA
[2]Department of Botany and Plant Pathology, Oregon State University, Corvallis, OR, USA
[3]National Institute of Water and Atmospheric Research, Wellington, NZ
[4]School of the Environment, University of Auckland, Auckland, NZ
[5]Department of Marine Sciences, University of Otago, Dunedin, NZ
[6]Takuvik Joint International Laboratory, Université Laval, Quebec City, QC, CA

[*]To whom correspondence should be addressed; E-mail: horvat@brown.edu.

Areas covered in compact sea ice are often assumed to prohibit upper ocean photosynthesis. Yet under-ice phytoplankton blooms (UIBs) have increasingly been observed in the Arctic, driven by changes to the optical properties of Arctic sea ice as it has thinned and become more seasonal. Here we show the Southern Ocean can also support widespread UIBs. Using under ice-enabled BGC-Argo float data, we detail numerous high chlorophyll and particulate backscatter events below compact sea ice preceding seasonal ice retreat, classifying 16 distinct UIB events. Using joint light, sea ice, and ocean conditions obtained from the ICESat-2 laser altimeter and 11 climate model contributions to CMIP6, we find that more than 4 million square kilometers of the compact-ice-covered Southern Ocean could support these events in late spring and early summer.

1 Introduction

Observations of under-ice phytoplankton blooms (UIBs) in the Arctic Ocean [1] have highlighted the need to understand ecological communities living under compact (local concentration greater than 80%) sea ice, now and under future climate change scenarios [2, and references within]. Regions supporting UIBs in the Arctic have likely expanded as sea ice has thinned and become more seasonal. Yet to date, no studies have quantified the potential for widespread UIBs under Antarctic sea ice, where annual and seasonal variability has changed less than in the Arctic over the satellite period [3] and where sea ice is typically thinner, more seasonal, and more fragmented.

Antarctic sea ice typically has a higher albedo than Arctic sea ice [4, 5]. Thus a limited amount of photosynthetically available radiation (PAR, 400-700 nm) can reach the upper ocean directly through sea ice, especially compared to the Arctic, where light transmission through melt-pond-covered sea ice is thought to be a primary cause of UIBs [6]. Still, spring-summer solar irradiance is high: recently a bloom of nanoflagellates was observed under highly reflective landfast sea ice [7]. Floating sea ice in the Southern Ocean is also fractured, thin, and mobile. Small areas of open water, like leads or small openings within the floe mosaic, can allow substantial amounts of light to reach the upper ocean. Sunlight entering the ocean through leads in the Arctic has been shown to initiate phytoplankton blooms, even in areas where sea ice is thick and snow-covered [8]. We therefore investigate this possibility across the sea-ice-covered Southern Ocean.

Phytoplankton communities in the Southern Ocean respond rapidly to changes in light conditions, with phytoplankton blooms often observed as soon as the sea ice edge retreats in spring, flooding the mixed layer with light and leaving freshwater rich in iron, main limiters of primary production [9, 10, 11]. In the Arctic, a crucial factor in the development of UIBs is a stable

surface mixed layer, which can be induced by melt water and/or increased solar heating of the surface layer [12, 13]. Observations using tagged seals in the Ross Sea show the initiation of a shallow (20 m) surface mixed layer driven by ice melt, preceding the seasonal retreat of sea ice [14]. Yet while shallow mixed layer depths may be necessary to keep phytoplankton in the well-lit surface layer, observations from under-ice Argo floats [15, 16] demonstrate that primary production can be initiated before seasonal sea ice retreat, and even before the restratification of surface waters. This challenges the notion that too-deep surface mixed layers in ice-covered regions of the Southern Ocean limit productivity. Together these factors present the possibility that non-coastal regions of the Southern Ocean, like the Arctic, may be productive before sea ice retreats in summer.

Here we assess the potential for widespread phytoplankton growth under compact (and floating) sea ice in the Southern Ocean. We examine 39 BGC-Argo floats that operated under sea ice in the Southern Ocean, 30 of which returned profiles under compact sea ice in austral spring-summer. Of these 30 floats, 27 recorded sub-surface Chl-a maxima that exceeded 0.1 mg/m^3. A further 12 recorded Chl-a values that exceeded 0.5 mg/m^3, which we define as a UIB, a threshold used to define UIBs in the seasonally ice-covered Arctic [17, 18, 19]. In total, we observed 28 UIB profiles in 16 distinct locations and time periods. To evaluate the general ability of the ice-covered Southern Ocean to permit UIBs, we combine ICESat-2 laser altimetry and 11 climate model assessments of Southern Ocean sea ice, light and ocean conditions, finding the conditions required for light-limited phytoplankton blooms are predicted across nearly 50% of regions with compact ice in spring and summer. These results suggest that in compact, but not completely ice-covered regions of the Southern Ocean, enough light reaches into the upper water column to permit primary production, as found in the Arctic [8]. We identify potential sampling regions for examining under-ice primary production and community composition in the Ross Sea, and discuss the implications for sampling strategies and cruise timing.

2 Observations of phytoplankton blooms under compact sea ice

Figure 1(a) scatters the maximum Chl-a measurement for BGC-Argo profiles (Chl_{max}, see methods) in the months of September to December when local sea ice concentration (SIC) exceeds 80%, overlaid on September-November climatological SIC. Due to the east of interpretation, we define high-productivity measurements using Chl_{max}, however Chl-a is an imperfect measure of phytoplankton biomass because it varies due to photoacclimation, nutrient conditions and growth stage, and several studies have identified uncertainty with Argo float fluorometers [20, 21]. For consistency with previous BGC-Argo work [22], and to support Chl_{max} observations, we compare Chl_{max} measurements with particulate backscattering data (b_{bp}, at 700nm, units m^{-1}) taken at the depth of maximum Chl-a. We found comparable seasonal cycles under compact ice and a high association (Spearman's R=0.7) between the two (see Supporting Information, Fig. S2). Example profiles of Chl-a and b_{bp} are provided as Supporting Figure S4 with Chl_{max} varying from 0.1 to 3.5 mg/m^3, showing the typical covariance of b_{bp} with Chl-a. The depth of Chl-a maxima are predominantly within the top 60 meters of the water column (Supporting Figure S3), implying the association between high Chl-a values and high particle concentrations is not due to photoacclimation.

In total, we considered 39 BGC-Argo floats that recorded 1153 profiles under sea ice in the Southern Ocean, 903 of which were under compact sea ice. 33 floats recorded 549 profiles during the period from September-December, of which 30 recorded 426 profiles under compact sea ice. Of these 30, 27 recorded Chl_{max} greater than 0.1 mg/m^3, indicating some photosynthetic activity, and 12 record Chl_{max} greater than 0.5 mg/m^3 at least once, a threshold we take to represent initiation of a under-ice "bloom". We note that we define blooms here only in a relative sense to background concentrations in the Southern Ocean (i.e, not relative to the North Atlantic

bloom) [20, 23]. The three floats recording profiles under compact ice in spring-summer that did not observe a value of Chl_{max} above 0.1 mg/m^3 accounted for just 14 total profiles, with just one under compact sea ice.

Many of the highest Chl_{max} values were recorded under compact sea ice. Considering 549 under-ice profiles taken between the months of September-December, we show box plots of Chl_{max} in Figure 1(b), grouped by sea ice concentration (SIC, in 20% bin intervals). A total of 52 profiles under sea ice recorded Chl_{max} above 0.5 mg/m^3: 11 for SIC from 20%-40%, 6 for SIC from 40% to 60%, 13 for SIC from 60% to 80%, and 28 for SIC from 80% to 100% (compact ice). Median Chl_{max} values are below 0.2 mg/m^3 in each SIC category, with the median for SIC from 20%-40% (0.15 mg/m^3, n=31) similar to that for SIC from 80-100% (0.12 mg/m^3, n=426).

Box plots of Chl_{max} in each month are given in Figure 1(c) for the 903 total profiles under compact sea ice. The seasonal cycle in median Chl_{max}, matches the seasonal cycle of downwelling solar irradiance. Median Chl_{max} under compact ice ranged from 0.03 mg/m^3 (n=163) in August, to a high of 0.38 mg/m^3 in December (n=24). The number of recorded Chl_{max} values exceeding 0.5 mg/m^3 was 0 through September, 3 out of 149 profiles in October, 17 out of 99 profiles in November, and 8 out of 24 profiles in December. These 28 "bloom" Chl-a measurements averaged 1.34 mg/m^3, were recorded by 12 different floats, and were under an average SIC of 94%. As BGC-Argo float records can span multiple years, these "bloom" measurements were recorded in 16 distinct times and locations. We found 7 instances where at least 2 successive profiles (Argo dives are spaced 10 days apart) recorded both $\text{Chl}_{max} > 0.5$ mg/m^3 and SIC$>$80%. Of the 7 "events" spanning 10 or more days, 6 included profiles taken in November - the other spanned only the month of December.

3 The prevalence of blooms under Antarctic sea ice

The presented BGC-Argo float data showed numerous elevated Chl-a events under compact sea ice in the Southern Ocean, and we found 16 distinct instances of Chl-a concentrations exceeding 0.5 mg/m^3 that were recorded under sea ice with an average SIC of 94%. Many of these high-Chlorophyll events were recorded in November, when Antarctic sea ice is near its seasonal maximum extent. We next quantify if conditions that support UIBs are widespread across the sea-ice covered Southern Ocean before sea ice retreat.

In Figure 2(a), we show ICESat-2-(IS2)-derived average ocean surface PAR values in the Southern Ocean in November, in which we make the simplifying assumption that no PAR reaches the upper ocean directly through sea ice (see methods). A solid line outlines the compact sea ice zone (CIZ, SIC $> 80\%$) defined using the NSIDC-CDR SIC product [24]. We also plot the 15% SIC contour, marking the edge of total sea ice extent (SIE). Regions lying inside the SIE contour but outside the CIZ are defined as marginal ice zones (MIZs), which due to the lower albedo of open water, receive higher PAR in the surface water layer compared to the CIZ. Figure 2(b) shows pre-industrial November PAR values for the CESM2 climate model (see methods), with CIZ and MIZ defined from the CESM2 model climatology. Both IS-2 and CESM2 show large areas within the CIZ where ocean surface PAR estimates exceed a "bloom" threshod of 23 μmol photons/m^2/s (see methods). For the IS-2 estimate of ocean surface PAR, 6.9 million km^2 of the November CIZ exceeds that PAR threshold, versus 5.9 million km^2 for CESM2. Because we do not have coincident ocean and sea ice melt observations at the scale of IS2 observations, IS2 estimates only indicate the presence of light in the upper ocean and may overestimate the area that permits an UIB.

We next consider how frequently an individual grid cell would permit an UIB (see methods), a metric we term the UIB%. A spatial map of UIB% in November months is given in Figure 2(c)

for CESM2. Areas within the climatological November CIZ (solid line), which has an area of 8.3 million km^2, permit an UIB 46.4% of the time. Because of year-to-year variability of the CIZ contour, areas outside of the climatological CIZ also have non-zero UIB%. In those areas, average UIB% is 19.3%. We accumulate climatological statistics of UIB-permitting regions in Figure 2(d), comparing the climatological extent of compact sea ice (red) to the extent of UIB-permitting regions (blue). Large areas support UIBs, peaking at 5.9 million km^2 of compact ice-covered regions in November. The fraction of the CIZ that permits an UIB, the UIB fraction (UIBF), is examined in Figure 2(d) (black line, right axis), which peaks in November at an UIBF of 77%. By point of comparison, we reproduce Figure 2(d) as Figure 2(e) for the Arctic Ocean. Up to 4.3 million km^2 of the pre-industrial Arctic CIZ is permissive to UIBs, repeating the finding in [2], that large regions of the pre-industrial Arctic also supported UIBs. The seasonal maximum of Arctic UIB area occurs in June, at the peak of the solar cycle, with a peak UIBF of 52% in July. Generally, in the CESM2 picontrol experiments, we find that UIB-permitting regions in the Antarctic are (1) larger, (2) constitute a larger percentage of the CIZ, and (3) peak earlier in the annual solar cycle (November in the Antarctic versus June in the Arctic) than in the Arctic.

Southern ocean UIB statistics across CMIP6 models

In Figure 3(a,b), we plot the climatological seasonal cycle of Southern Ocean UIB area (a) and UIBF (b) for the 11 CMIP6 models (listed in Supporting Table S2). Across these models, we find a similar seasonal cycle. None of the CMIP6 models have large UIB areas before October, but 10 of 11 have a maximum UIB area in November. Only the MRI-ESM2 model shows a maximum UIB area in December. Each has a climatological UIB area exceeding 2.66 million km^2, with a median of 4.75 million km^2. In Figure 3(c), we show box plots of annual maximum UIB area in the Antarctic for each of the models (filled), compared to annual maximum UIB

area in the Arctic (unfilled) for the same years. Out of 11 models, 8 have median Antarctic UIB areas that exceed Arctic UIB areas.

We repeat Figure 3(a,c) in Figure 3(b,d) for the UIBF, with Figure 3(d) showing UIBF values during the month where UIB area is at its maximum (November or December in the Antarctic, June or July in the Arctic). Seasonal cycles of UIBF are similar between models, with most models peaking in December as the CIZ reduces in extent and ocean surface PAR increases. In 10 of 11 models, a higher fraction of the Antarctic CIZ permits an UIB than of the Arctic CIZ. Average values of UIBF range from 27-86% (average 57%) in the Antarctic, compared to 26-66% in the Arctic (average 37%). Each of the three models in which Antarctic UIB areas were less than Arctic UIB areas have higher UIBF in the Antarctic. Thus we suggest that the reason for differences in the overall magnitude of Antarctic UIB areas is due to differences in model representations of Antarctic and Arctic sea ice, not disagreements about whether sufficient PAR is available under the compact sea ice there.

4 The potential for observing UIBs in situ

Using BGC-Argo float data, we have demonstrated that high phytoplankton biomass events exist under compact sea ice in the Southern Hemisphere, preceding the seasonal loss of sea ice by several months. Examining a series of climate model estimates of upper ocean light and sea ice conditions, we found that under-ice phytoplankton growth is permitted across wide swaths of the compact ice-covered Southern Ocean. We also found that areas permitting UIBs make up a larger percentage of compact sea ice zones in the Southern Ocean than the Arctic, with an earlier peak in the seasonal cycle. To validate these results further, observational campaigns will be needed. We specifically focus on the potential of the Ross Sea region (see methods) to support such an event, as it is seasonally ice free, and is among the highest-productivity regions of the Southern Ocean, and is known for supporting large ice-algal communities [25, 26].

In Figure 4, we plot UIB% for each of the 11 models during the model period with highest Ross Sea UIB area, which is November in 7 models and December in 4 models. All models have high UIB% in the coastal region near Cape Adare in the Western Ross Sea, which has compact sea ice into January. We identify a region at 72°S, 178.5°E with a blue square in Figure 4. A box plot of UIB% in this location for these 11 models is given in Figure 4 (bottom right), showing a median UIB% there of 62% with a minimum of 40%. Across the CMIP6 models, a mean area of 0.55 million km^2 of the Ross Sea is expected to permit UIBs, although the borders of UIB-permitting areas vary by model, and range from 0.29 million km^2 (MRI-ESM2, 49% of the Ross CIZ) to 0.95 million km^2 (NorESM2-LM, 65% of the Ross CIZ), with inter-annual variability. Independent of modeled sea-ice area coverage, a large fraction of the Ross CIZ permits UIBs in each year in all models. Figure 3 is repeated as Supporting Figure S1 for the Ross Sea region, showing that during the month of highest Ross Sea UIB area, at least 49% of the Ross CIZ permits UIBs in each model, on average 60%.

5 Discussion

Here we explored the potential for under-ice phytoplankton blooms beneath compact sea ice in the Southern Ocean using model simulations, altimetric measurements of sea ice coverage, and BCG-Argo data. We show that on at least 16 distinct occasions from October-December, BCG-Argo floats recorded Chl-a concentrations above 0.5 mg/m^3 in areas with an average sea ice concentration of 94%. In addition to these direct high Chl-a measurements, findings of elevated (Chl$_{max}$ $>$ 0.1 mg/m^3) Chl-a concentrations in a large fraction of analyzed float data demonstrates the likelihood for primary production and blooms beneath Antarctic sea ice predating seasonal sea ice retreat. These elevated levels of Chl$_{max}$ under compact ice suggest that even for areas with low open water fraction, incident solar radiation is high enough to promote photosynthetic activity. This is similar to findings in the Arctic where small lead features

were sufficient to support under-ice blooming [8], and suggests that small regions of open water are sufficient to relax light limitations on blooming in the summertime Southern Ocean. We supplemented the Chl-a observations with observations of b_{max}, values of particulate backscatter b_{bp} taken at the same depth as Chl_{max}. We find high association between Chl-a and b_{max} (Spearman's R = 0.7, see Supporting Info Fig. S2), reinforcing that these high Chl-a events are associated with higher particle (i.e., biomass) concentration in the water column.

We further used ICESat-2 and an ensemble of climate model estimates of sea ice, light, and oceanographic conditions across the compact-ice-covered Southern Ocean to show that indeed, conditions are favorable for under-ice blooms over wide regions, with a median estimate UIB area of 4.75 million km^2 across the model ensemble. In using ICESat-2 data, we assumed that no light reached through sea ice, and all light available for photosynthesis came through open water regions near compact ice. Thus these findings indicate that even in regions with local sea ice concentrations above 80%, and with no light passing directly through the ice, enough open water exists that light does not limit growth in the upper Southern Ocean [16]. As modeled and observed in the Arctic, such widespread under-ice productivity, preceding the retreat of seasonal sea ice, may reveal a markedly different ecological system than was previously understood to exist there. Since sea ice conditions in the Antarctic have not changed dramatically over the global warming period, under-ice phytoplankton may play an important role in driving or limiting blooms observed to occur when sea ice retreats.

The climate models considered here have inter-related sea ice and light schemes (see Supporting Table S2), and provide estimates of the light conditions in the Southern Ocean. They may not be accurate if systematic biases in modeled Southern Ocean climate or sea ice properties exist. Still, compared against the estimate of upper ocean PAR derived from ICESat-2 data, models produce similar PAR estimates and areas of high surface light levels. We adopted a simple diagnostic criteria for when sufficient light is available to support a bloom, using a fixed

PAR threshold in model data, in line with Arctic model studies and observations of acclimation in key Antarctic phytoplankton species [27]. While some BGC-Argo floats do report PAR values, their ice-avoidant algorithms mean near-surface PAR was not observed - and further observations and modeling of radiative transfer of PAR specifically focused on variable Antarctic sea ice (as in, for example, [28, 29]) would help constrain and evaluate PAR levels needed to trigger blooms in concert with BGC-Argo data. While the Argo data confirms that under-ice regions can be productive, because of their uneven spatial and temporal coverage (Supporting Info Fig. S3), it is not yet possible to directly compare geographic estimates of model-predicted conditions to float data. Thus here we use the Argo data in conjunction with models for understanding the possibility of under-ice blooms, but cannot directly validate model predictions of pan-Antarctic UIB extents.

The work we presented here raises an important question: if conditions beneath compact sea ice are favorable for supporting UIBs, and Antarctic sea ice coverage and downwelling irradiance has remained largely stable over the past several decades, why are there no reported observations of under-ice blooms in the Southern Ocean by underway cruises or moorings? We suggest two potential answers.

First, the detection of UIBs requires a dedicated effort to collect in situ chlorophyll data under compact sea ice. An analogy can be drawn to the Arctic Ocean, where spring-summer icebreaker research expeditions are more common. UIBs are now thought to have been widespread dating back to at least the 1950s (with an overall area coverage that has doubled since 1970 [2]). But these phenomena, which can have some of the highest levels of integrated biomass of any ecological system [1], were rarely observed before the report of a massive under-ice bloom in the Chukchi Sea in 2011. As we show here, BGC-Argo floats permit a broader sampling of biological parameters across the Southern Hemisphere using consistent methodologies and calibrations. Mining of existing and previous under-ice Chlorophyll data, for example from the

BCO-DMO archive, will be a focus of future work to understand whether such events have been observed in the past.

Second, it is possible that UIBs do not occur regularly. While nearly all BGC-Argo floats operating from September-December show elevated Chl-a measurements predating sea ice retreat, only 28 profiles, from 12 of 30 floats operating in the right time and sea ice conditions, exceed our defined Chl-a threshold for a "bloom", which here is defined relative to typical open water and under-ice conditions in the Southern Ocean [20, 23]. Of these, we recorded 7 events with two or more subsequent measurements meeting the "bloom" threshold. These multi-measurement events occurred in December 2014 (Argo id 5904180), November-December 2016 (Argo id 5904767 and 5904180, which was previously discussed in [30]), October-November 2017 (Argo ids 5905100 and 5904180), November 2019 (Argo id 5905379), and November-December 2018 (Argo id 5905636). Further research into these specific events will be necessary to rule out that the high levels of Chl-a recorded by these floats were not, for example, advected from a bloom occurring in open water. Our assessment of favorable underwater light conditions for UIBs over large areas of the compact ice zone is also based on a simple set of diagnostic criteria, not detailed biogeochemical modeling, and uses bulk estimates for light transmission and stratification. We do not take into account iron or other nutrient limitations, nor grazing pressure by higher trophic levels. Instead we follow the perspective of [11] that primary production is primarily light-limited in summer. Thus the UIB-permitting area of the Southern Ocean in this study is likely an upper bound on the areas that might bloom in a given year.

This work suggests there is potentially unexplored ecological variability beneath Southern Ocean sea ice, with several million square kilometers of the ice-covered Southern Ocean potentially permitting blooms before the seasonal retreat of the sea ice edge. We paid special attention to the frequently visited Ross Sea region, and suggest detailed measurements

of physical and biogeochemical variables to study under-ice phytoplankton bloom phenology, magnitude and community composition and to compare those to known bloom dynamics in the Arctic Ocean [31]. Sampling during the sea ice-covered season will be challenging, especially as remote sensing technologies presently cannot measure chlorophyll under sea ice. Continued targeted deployment of Remotely Operated Vehicles (ROV) and other autonomous profiling floats [15, 16] to measure under-ice light availability and bio-optical parameters can be complementary to ship-based sampling, supported by ICESat-2 measurements used to remotely sense particulate backscatter in ice-free conditions [32] extended into sea-ice-covered regions.

6 Methods

Ice-enabled BGC-Argo float data Autonomous profiling Argo floats equipped with biological sensors are a foundation of Southern Ocean biogeochemical observations because they provide observations with consistent sampling methodologies in places (and at sampling frequencies) inaccessible via ships, and with depth resolution inaccessible via satellite, while experiencing minimal biofouling and lateral drift [33]. Because Argo floats drift with the currents during their transit, a portion of floats deployed in open water drift into ice-covered regions. To protect the floats from ice damage, an ice-avoidant algorithm (based on a temperature threshold) was implemented to initiate a float's descent when it encounters near freezing surface waters [34]. We used Chl-a flourescence data and particulate backscattering data b_{bp} (700 nm) collected with biogeochemical Argo floats (BGC-Argo) [35], which have been shown to be consistent with both satellite-derived Chl-a and in situ Chl-a values measured via High Performance Liquid Chromatography in the Southern Ocean [20, 21] following bias and non-photochemical quenching corrections [36] . In this study we use quality controlled and calibrated [21] delayed-mode data distributed through SOCCOM. Parameters for the floats are sampled at 2m vertical resolution. We did not impose geographical constraints on the data, and required only that float data come from compact (SIC $> 80\%$) regions in the Southern Ocean.

Chl-a observations are supported by particle backscatter (b_{bp}) data because while Chl-a is a pigment common to all phytoplankton, its observed value varies can vary based on both phytoplankton physiology and measurement error. Particulate backscattering covaries with phytoplankton biomass as phytoplankton scatter light proportional to their concentration and size [37], although b_{bp} observations do not necessarily imply the presence of phytoplankton because b_{bp} can be elevated due to the presence of non-algal particles. Backscatter has been shown to be a better proxy for phytoplankton carbon compared to Chl-a ([38] with Argo floats having less

measurement uncertainty for b_{bp} (on the order of 15%), [39] than for Argo Chl-a.

As in [39, 40], all float profiles of Chl-a and b_{bp} (700 nm, m^{-1}) were despiked with a 3-point moving median and we visually confirmed that maximum Chl-a values were not from noise in the profile. We report the maximum adjusted Chl-a, Chl_{max}, within a profile due to unavailable profile data near the surface (float descended prior to reaching the surface due to the ice avoidant algorithm, see also [41]). Examples of four Chl-a and b_{bp} profiles are given in Supporting Figure S4. We also examine values of b_{max}, the value of b_{bp} at the depth of Chl_{max}, to confirm that the high Chl-a is due to phytoplankton, with Fig. 1(a) repeated as Fig. S2(b) for b_{max}. Profiles of Chl-a are not considered if Chl_{max} is recorded at a depth above 200 meters, or if b_{max} exceeds 0.01 m^{-1}, which exceeds natural values of b_{bp} found in phytoplankton and possibly reflects the influence of bubbles or large particles (zooplankton) that were attracted to the instrumentation [42].

Maximum values of Chl-a reported here may represent an underestimate of the true maximum Chl-a in the water column, as it is not possible to assess Chl-a concentrations closer to the surface under sea ice because of the ice-avoidant nature of the Argo floats, and typically ocean phytoplankton blooms are surface-intensified [1, 43]. For example, the mean depth of Chl_{max} for the 28 profiles with Chl_{max} above 0.5 mg/m^3 under compact ice was 45 meters. Location information for a float under sea ice is imprecise, as the latitude and longitude coordinates are calculated via a linear interpolation of the pre- and post-sea ice coordinates of a specific float. In some cases, the float will not surface in open water and post-sea ice coordinates are unavailable. Some floats lack under-ice geographic coordinates if they do not surface under open water conditions following a period under ice. Thus it is not possible to interpolate all float location while it transits an ice-covered region, and we remove such floats/dives.

This study includes under-ice profiles initially obtained from 41 BGC-Argo floats. To obtain sea ice concentrations (SIC) in the area of float deployment, we matched geographic coordinates

for each float to the daily 25-km resolution NSIDC Climate data record SIC product [24]. We excluded locations with a local estimated SIC below 15%, and outlier profiles where b_{bp} at the depth of maximum Chl-a exceeded 0.01 m^{-1}. In total, that leaves 1153 profiles under sea ice from 39 floats. Of all profiles, 35 floats recorded 903 profiles with local SIC above 80% in all months. Of all profiles, 33 floats recorded 549 profiles during the months of September-December. Combining these criteria, 30 floats recorded 426 profiles with local SIC above 80% between September and December. A list of all floats is provided in the Supporting Information Table S2.

CMIP6 model data Remote sensing technologies presently do not directly measure light or chlorophyll beneath sea ice, and most sampling strategies for Southern Ocean photosynthetic communities associated with sea ice focus on in-ice algae communities in coastal regions [44, 45, 46, 47]. We must instead turn to model estimates to describe the joint climatological light, sea ice, and ocean conditions underneath sea ice. We used an ensemble of current-generation coupled climate models contributing to the 6th Coupled Model Intercomparison Project (CMIP6).

While observations show Antarctic sea ice has been stable or increased in extent over the satellite period (1978-present), CMIP6 models consistently simulate a declining annual-average Antarctic sea-ice cover over this period [48]. Thus we did not consider it feasible to examine present-day model estimates of Antarctic sea ice state, which might incorporate biased depictions of sea ice albedo and extent. Instead we postulate that light conditions under Antarctic sea ice have remained stable over the industrial period, and use data from pre-industrial control run simulations (CMIP6 runs titled picontrol) in this analysis. Of the full CMIP6 model dataset, 11 simulations (see Supporting Table S1) submitted the required model output we used here.

The ensemble of 11 models produced variable estimates of climate and sea ice state, de-

spite high interrelation between their sea ice and radiative transfer model components. Different versions of the Community Sea Ice Model (CICE) are used as sea ice model components in 9 of 11 models. There are three substantively different light models, the improved [49] (B+L) δ-Eddington multiple-scattering scheme found in CICE versions 5 and above (CESM2 and NorESM2 simulations), an earlier version of the B+L scheme found in CICE version 4 (CAS), or implementations of simpler Beer-Lambert exponential attenuation of light in ice (CERFACS,MRI).

For each CMIP6 model, we defined a climatology of light and sea ice properties using the final 100 years of their respective pre-industrial spinup experiments. In Fig. 2 we specifically examined the Community Earth System Model version 2 (CESM2, [50]) model run, as it uses the more recent version of CICE and the more advanced B+L δ-Eddington light scheme. CESM2 produces an overall mean state of Antarctic sea ice that is broadly realistic compared to other CMIP6 models [48, 51], and similar output from CESM2 was analyzed to evaluate the potential for Arctic UIBs in [2].

ICESat-2 light data To supplement model estimates of light under sea ice, we approximated the light field under sea ice using the ICESat-2 laser altimeter. We utilized the L3A along-track sea ice type product (ATL07, [52]) derived from Level 2A ATL03 photon heights [53]. Sea ice types are determined using an empirical decision tree, which identifies whether a given segment is sea ice or water. We developed an estimate of SIC as the ratio of total ice segment length to total segment length. This quantity, the linear concentration c^*, is related to the SIC, defined over a 2-dimensional region. Given the random orientation of crack and open water features relative to frequent satellite tracks, many repeat 1-D measurements can approximate a 2-D field when sampled sufficiently. In [54], we found global sea ice area metrics derived from passive microwave (PM) satellites were well-approximated by this method in regions where IS2 records

at least 1000 individual segments per month. We adopted this same threshold in this study to define c^*. An advantage of using ICESat-2 segments instead of PM is that ICESat-2 is capable of resolving small cracks and leads that are difficult to observe in PM estimates of local SIC, particularly in summer [55, 56, 57].

From a gridded dataset of c^*, we estimated the total shortwave irradiance, I_0 ($\sim$ 300–3000 nm), reaching the upper ocean, I_0,

$$I_0 = SW(1 - c^*)(1 - \alpha_{oc}) \tag{1}$$

where $\alpha_{oc} = 0.06$ is the open water albedo and SW is the downwelling solar irradiance at the surface. This shortwave irradiance is then converted to a PAR (400-700 nm) estimate as in the CMIP6 model data (see methods below). This simple model assumes no light passes through the sea ice surface, and the only light available in ice-covered regions comes through the open water part of the area. For this reason we expect ICESat-2 derived downwelling irradiances may be conservative. For SW, we use the reanalyzed estimate of downwelling shortwave irradiance from [58]. We use IS2 data from January 2019-December 2020 to form the present-day climatology of I_0 that is presented in Figure 2.

Criteria for permitting an UIB We define an area as "permitting" an under-ice bloom if it meets three criteria:

Compact sea ice Local sea ice concentration exceeds 80%.

An illuminated upper ocean. Average PAR in the top 25 meters of the ocean exceeds 10 μmol photons/m^2/s.

A stable or stratifying surface mixed layer. Sea ice is not refreezing and the upper ocean is non-convecting.

The UIB% is therefore defined as the percentage of model years where a grid cell meets all three criteria together. Thus the UIB% can be low if a region both if it is not frequently covered by compact sea ice, or if the light conditions and ocean stratification are not permissive of a bloom.

We focused on those ocean regions under "compact" sea ice to differentiate from phytoplankton growth known to occur as the ice edge retreats in marginal ice zones [59, 60]. Marginal ice zones are typically defined as areas where sea ice concentration is less than 80% [61, e.g.,], thus we used this cutoff to define regions that are "compact" ice.

To establish a threshold for upper-ocean PAR, we estimated average PAR, $\overline{I}$, at a depth D as,

$$\overline{I} = \frac{I_0}{\kappa D}\left[1 - \exp(-\kappa D)\right]. \tag{2}$$

Here we assumed that PAR is attenuated exponentially in water with a coefficient κ. We assumed positive photosynthesis (gains outweigh losses) occurs when the average PAR over a 25-m deep water column exceeds 10 μmol photons / m$^2/s$. This is approximately twice the threshold of integrated daily irradiance of 4.8 μmol photons / m$^2/s$ considered to initiate a phytoplankton bloom in [62, 63, 13], and higher than the levels found to initiate growth in the Southern Ocean [15, 16]. Using $\kappa = 0.081/m$ [64] for PAR extinction in clear waters and $D = 25$ m established a PAR threshold value for blooms of $I_0^* \approx 23$ μmol photons /m^2/s. CMIP6 models typically store and output full-spectrum solar forcing to the upper ocean, but not PAR. We therefore had to convert full spectrum solar irradiance to PAR using a factor of 1.9975 μmol photons/J [65, 64].

We also included a threshold for the termination of upper-ocean convection. Under-ice blooms are unlikely to occur when active convection extends below the euphotic zone, such as when leads are actively refreezing with the ocean at its freezing point [12]. The requirement that the upper ocean is non-convecting is similar to the "turbulent shutdown" theory used to

explain mid-latitude phytoplankton blooms [66]. GCMs used here are too coarse to resolve the complex boundary layer dynamics that result from surface melting of sea ice [67, 68, 69], and thus they are not suited for determining the convective state of the upper ocean in the presence of sea ice leads. Instead, we considered the ocean to be non-convecting if sea ice was melting at its base, which would lead to stratification of the upper ocean, consistent with Argo observations of high negative covariance between shoaling MLD and phytoplankton biomass under ice [41]. In practice, simply non-zero basal melting does not restrict the location of UIBs as small monthly-averaged basal melt rates occur whenever sea ice is present. We therefore set a positive threshold for the sea ice basal melt rate $\dot{h}$, which we expressed as an equivalent heat flux $Q = \rho_i L_f \dot{h}$, with ρ_i = 920 kg/m^3 the sea ice density and $L_f = 3.34 \times 10^{-5}$ J/kg the latent heat of fusion. As a result Q is required to exceed 5 W/m^2, for an approximate basal melt rate of $\dot{h} = 5$ cm/month.

The Ross Sea region To define the "Ross Sea region", we roughly followed the convention established by the NIWA Ross Sea Trophic Model [70], taking the ocean region south of 69°S and between 160°W and 170°E longitude. Because of grid variations, the area of this region can vary between CMIP6 models, but its surface area is approximately 1.5 million km^2.

References

[1] Arrigo, K. R. *et al.* Massive Phytoplankton Blooms Under Arctic Sea Ice. *Science* **336**, 1408 (2012). URL http://www.sciencemag.org/cgi/doi/10.1126/science.1215065.9605103.

[2] Ardyna, M. *et al.* Under-Ice Phytoplankton Blooms: Shedding Light on the "Invisible" Part of Arctic Primary Production. *Frontiers in Marine Science* **7**, 1–25 (2020). URL

https://www.frontiersin.org/articles/10.3389/fmars.2020.608032/full.

[3] Parkinson, C. L. A 40-y record reveals gradual Antarctic sea ice increases followed by decreases at rates far exceeding the rates seen in the Arctic. *Proceedings of the National Academy of Sciences of the United States of America* **116**, 14414–14423 (2019).

[4] Brandt, R. E., Warren, S. G., Worby, A. P. & Grenfell, T. C. Surface Albedo of the Antarctic Sea Ice Zone. *Journal of Climate* **18**, 3606–3622 (2005). URL https://journals.ametsoc.org/jcli/article/18/17/3606/30648/Surface-Albe

[5] Arndt, S. *et al.* Influence of snow depth and surface flooding on light transmission through Antarctic pack ice. *Journal of Geophysical Research: Oceans* **122**, 2108–2119 (2017). URL http://www.nature.com/articles/175238c0 http://doi.wiley.com/10.1002/2016JC012325.

[6] Arrigo, K. R. *et al.* Phytoplankton blooms beneath the sea ice in the Chukchi sea. *Deep-Sea Research Part II: Topical Studies in Oceanography* **105**, 1–16 (2014). URL http://linkinghub.elsevier.com/retrieve/pii/S0967064514000836.

[7] Saggiomo, M., Escalera, L., Saggiomo, V., Bolinesi, F. & Mangoni, O. Phytoplankton Blooms Below the Antarctic Landfast Ice During the Melt Season Between Late Spring and Early Summer. *Journal of Phycology* **57**, 541–550 (2021). URL https://onlinelibrary.wiley.com/doi/10.1111/jpy.13112.

[8] Assmy, P. *et al.* Leads in Arctic pack ice enable early phytoplankton blooms below snow-covered sea ice. *Scientific Reports* **7**, 40850 (2017). URL http://www.nature.com/articles/srep40850.

[9] Martin, J. H., Fitzwater, S. E. & Gordon, R. M. Iron deficiency limits phytoplankton growth in Antarctic waters. *Global Biogeochemical Cycles* **4**, 5–12 (1990). URL http://doi.wiley.com/10.1029/GB004i001p00005.

[10] Comiso, J. C., McClain, C. R., Sullivan, C. W., Ryan, J. P. & Leonard, C. L. Coastal zone color scanner pigment concentrations in the Southern Ocean and relationships to geophysical surface features. *Journal of Geophysical Research: Oceans* **98**, 2419–2451 (1993). URL http://doi.wiley.com/10.1029/92JC02505.

[11] van Oijen, T. Light rather than iron controls photosynthate production and allocation in Southern Ocean phytoplankton populations during austral autumn. *Journal of Plankton Research* **26**, 885–900 (2004). URL https://academic.oup.com/plankt/article-lookup/doi/10.1093/plankt/fbh08

[12] Lowry, K. E. *et al.* Under-Ice Phytoplankton Blooms Inhibited by Spring Convective Mixing in Refreezing Leads. *Journal of Geophysical Research: Oceans* **123**, 90–109 (2018). URL http://doi.wiley.com/10.1002/2016JC012575.

[13] Oziel, L. *et al.* Environmental factors influencing the seasonal dynamics of spring algal blooms in and beneath sea ice in western Baffin Bay. *Elementa: Science of the Anthropocene* **7**, 34 (2019). URL https://online.ucpress.edu/elementa/article/doi/10.1525/elementa.372/11

[14] Porter, D. F. *et al.* Evolution of the Seasonal Surface Mixed Layer of the Ross Sea, Antarctica, Observed With Autonomous Profiling Floats. *Journal of Geophysical Research: Oceans* **124**, 4934–4953 (2019).

[15] Arteaga, L. A., Boss, E., Behrenfeld, M. J., Westberry, T. K. & Sarmiento, J. L. Seasonal modulation of phytoplankton biomass in the Southern Ocean. *Nature Communications* **11** (2020). URL http://dx.doi.org/10.1038/s41467-020-19157-2.

[16] Hague, M. & Vichi, M. Southern Ocean Biogeochemical Argo detect under-ice phytoplankton growth before sea ice retreat. *Biogeosciences* **18**, 25–38 (2021). URL https://bg.copernicus.org/articles/18/25/2021/.

[17] Apollonio, S. Hydrobiological measurements on IGY drifting station Bravo. *Trans. Am. Geophys. Union* **40**, 316–3 (1959).

[18] Laney, S. R. *et al.* Assessing algal biomass and bio-optical distributions in perennially ice-covered polar ocean ecosystems. *Polar Science* **8**, 73–85 (2014). URL https://linkinghub.elsevier.com/retrieve/pii/S1873965213000510.

[19] Boles, E. *et al.* Under-Ice Phytoplankton Blooms in the Central Arctic Ocean: Insights From the First Biogeochemical IAOOS Platform Drift in 2017. *Journal of Geophysical Research: Oceans* **125**, 6069–6079 (2020). URL https://onlinelibrary.wiley.com/doi/10.1029/2019JC015608.

[20] Haëntjens, N., Boss, E. & Talley, L. D. Revisiting Ocean Color algorithms for chlorophyll-a and particulate organic carbon in the Southern Ocean using biogeochemical floats. *Journal of Geophysical Research: Oceans* **122**, 6583–6593 (2017). URL https://onlinelibrary.wiley.com/doi/10.1002/2017JC012844.

[21] Johnson, K. S. *et al.* Biogeochemical sensor performance in the SOCCOM profiling float array. *Journal of Geophysical Research: Oceans* **122**, 6416–6436 (2017). URL https://onlinelibrary.wiley.com/doi/10.1002/2017JC012838.

[22] Mayot, N. *et al.* Assessing Phytoplankton Activities in the Seasonal Ice Zone of the Greenland Sea Over an Annual Cycle. *Journal of Geophysical Research: Oceans* **123**, 8004–8025 (2018). URL http://doi.wiley.com/10.1029/2018JC014271.

[23] Moore, J. K. & Abbott, M. R. Phytoplankton chlorophyll distributions and primary production in the Southern Ocean. *Journal of Geophysical Research: Oceans* **105**, 28709–28722 (2000). URL http://doi.wiley.com/10.1029/1999JC000043.

[24] Meier, W. N., Fetterer, F., Windnagel., A. K. & Stewart, J. S. NOAA/NSIDC Climate Data Record of Passive Microwave Sea Ice Concentration, Version 4. (2021).

[25] Lizotte, M. P. The Contributions of Sea Ice Algae to Antarctic Marine Primary Production. *American Zoologist* **41**, 57–73 (2001). URL https://academic.oup.com/icb/article-lookup/doi/10.1093/icb/41.1.57.

[26] Arrigo, K. R. Physical control of chlorophyll a , POC, and TPN distributions in the pack ice of the Ross Sea, Antarctica. *Journal of Geophysical Research* **108**, 3316 (2003). URL https://onlinelibrary.wiley.com/doi/10.1029/2001JC001138.

[27] Arrigo, K. R. *et al.* Photophysiology in two major southern ocean phytoplankton taxa: Photosynthesis and growth of phaeocystis antarctica and fragilariopsis cylindrus under different irradiance levels. *Integrative and Comparative Biology* **50**, 950–966 (2010).

[28] Horvat, C., Flocco, D., Rees Jones, D. W., Roach, L. & Golden, K. M. The Effect of Melt Pond Geometry on the Distribution of Solar Energy Under First-Year Sea Ice. *Geophysical Research Letters* **47** (2020). URL https://onlinelibrary.wiley.com/doi/abs/10.1029/2019GL085956.

[29] Katlein, C., Valcic, L., Lambert-Girard, S. & Hoppmann, M. New insights into radiative transfer within sea ice derived from autonomous opti-

cal propagation measurements. *The Cryosphere* **15**, 183–198 (2021). URL https://tc.copernicus.org/articles/15/183/2021/.

[30] Briggs, E. M., Martz, T. R., Talley, L. D., Mazloff, M. R. & Johnson, K. S. Physical and Biological Drivers of Biogeochemical Tracers Within the Seasonal Sea Ice Zone of the Southern Ocean From Profiling Floats. *Journal of Geophysical Research: Oceans* **123**, 746–758 (2018). URL https://onlinelibrary.wiley.com/doi/10.1002/2017JC012846.

[31] Chase, A. P. *et al.* Evaluation of diagnostic pigments to estimate phytoplankton size classes. *Limnology and Oceanography: Methods* (2020).

[32] Lu, X. *et al.* Antarctic spring ice-edge blooms observed from space by ICESat-2. *Remote Sensing of Environment* **245**, 111827 (2020). URL https://doi.org/10.1016/j.rse.2020.111827.

[33] Poteau, A., Boss, E. & Claustre, H. Particulate concentration and seasonal dynamics in the mesopelagic ocean based on the backscattering coefficient measured with Biogeochemical-Argo floats. *Geophysical Research Letters* **44**, 6933–6939 (2017). URL http://doi.wiley.com/10.1002/2017GL073949.

[34] Klatt, O., Boebel, O. & Fahrbach, E. A profiling float's sense of ice. *Journal of Atmospheric and Oceanic Technology* **24**, 1301–1308 (2007). URL http://journals.ametsoc.org/doi/abs/10.1175/JTECH2026.1.

[35] Claustre, H. *et al.* Bio-Optical Profiling Floats as New Observational Tools for Biogeochemical and Ecosystem Studies: Potential Synergies with Ocean Color Remote Sensing. In *Proceedings of OceanObs'09: Sustained Ocean Observations*

and Information for Society, 1, 177–183 (European Space Agency, 2010). URL http://www.oceanobs09.net/proceedings/cwp/cwp17.

[36] Roesler, C. *et al.* Recommendations for obtaining unbiased chlorophyll estimates from in situ chlorophyll fluorometers: A global analysis of WET Labs ECO sensors. *Limnology and Oceanography: Methods* **15**, 572–585 (2017). URL https://onlinelibrary.wiley.com/doi/10.1002/lom3.10185.

[37] Hergert, W. & Wriedt, T. *The Mie theory: basics and applications* (Springer, 2012).

[38] Graff, J. R. *et al.* Analytical phytoplankton carbon measurements spanning diverse ecosystems. *Deep Sea Research Part I: Oceanographic Research Papers* **102**, 16–25 (2015). URL https://linkinghub.elsevier.com/retrieve/pii/S0967063715000801.

[39] Bisson, K. M., Boss, E., Westberry, T. K. & Behrenfeld, M. J. Evaluating satellite estimates of particulate backscatter in the global open ocean using autonomous profiling floats. *Optics Express* **27**, 30191 (2019). URL https://www.osapublishing.org/abstract.cfm?URI=oe-27-21-30191.

[40] Bisson, K. M., Boss, E., Werdell, P. J., Ibrahim, A. & Behrenfeld, M. J. Particulate Backscattering in the Global Ocean: A Comparison of Independent Assessments. *Geophysical Research Letters* **48** (2021). URL https://onlinelibrary.wiley.com/doi/10.1029/2020GL090909.

[41] Bisson, K. M. & Cael, B. B. How are under ice phytoplankton related to sea ice in the Southern Ocean? *Geophysical Research Letters* 1–14 (2021). URL https://onlinelibrary.wiley.com/doi/10.1029/2021GL095051.

[42] Haëntjens, N. *et al.* Detecting Mesopelagic Organisms Using Biogeochemical-Argo Floats. *Geophysical Research Letters* **47** (2020).

[43] SMITH, W. O. & NELSON, D. M. Phytoplankton Bloom Produced by a Receding Ice Edge in the Ross Sea: Spatial Coherence with the Density Field. *Science* **227**, 163–166 (1985). URL http://www.sciencemag.org/content/227/4683/163.shorthttp://www.sciencem

[44] Smetacek, V. *et al.* Early spring phytoplankton blooms in ice platelet layers of the southern Weddell Sea, Antarctica. *Deep Sea Research Part A. Oceanographic Research Papers* **39**, 153–168 (1992). URL https://linkinghub.elsevier.com/retrieve/pii/019801499290102Y.

[45] Arrigo, K. R. & Thomas, D. N. Large scale importance of sea ice biology in the Southern Ocean. *Antarctic Science* **16**, 471–486 (2004).

[46] McMinn, A., Martin, A. & Ryan, K. Phytoplankton and sea ice algal biomass and physiology during the transition between winter and spring (McMurdo Sound, Antarctica). *Polar Biology* **33**, 1547–1556 (2010). URL http://www.nature.com/articles/175238c0 http://doi.wiley.com/10.1002/2016JC012325 http://link.springer.com/10.1007/s00300-010-0844-6.

[47] Cummings, V. J. *et al.* In situ response of Antarctic under-ice primary producers to experimentally altered pH. *Scientific Reports* **9**, 6069 (2019). URL http://dx.doi.org/10.1038/s41598-019-42329-0 http://www.nature.com/articles/s41598-019-42329-0.

[48] Roach, L. A. *et al.* Antarctic Sea Ice Area in CMIP6. *Geophysical Research Letters* 1–24 (2020).

[49] Briegleb, B. P. & Light, B. A Delta-Eddington multiple scattering parameterization for solar radiation in the sea ice component of the Community Climate System Model. Tech. Rep. February, National Center for Atmospheric Research (2007).

[50] Danabasoglu, G. *et al.* The Community Earth System Model Version 2 (CESM2). *Journal of Advances in Modeling Earth Systems* **12**, 1–35 (2020).

[51] Singh, H. K. A., Landrum, L., Holland, M. M., Bailey, D. A. & DuVivier, A. K. An Overview of Antarctic Sea Ice in the Community Earth System Model version 2, Part I: Analysis of the Seasonal Cycle in the Context of Sea Ice Thermodynamics and Coupled Atmosphere-Ocean-Ice Processes. *Journal of Advances in Modeling Earth Systems* (2020).

[52] Kwok, R. *et al.* ATLAS/ICESat-2 L3A Sea Ice Height, Version 1. Boulder, Colorado USA. Tech. Rep. May, NSIDC, Boulder, Colorado USA (2019).

[53] Neumann, T. A. *et al.* The Ice, Cloud, and Land Elevation Satellite – 2 mission: A global geolocated photon product derived from the Advanced Topographic Laser Altimeter System. *Remote Sensing of Environment* **233**, 111325 (2019). URL https://linkinghub.elsevier.com/retrieve/pii/S003442571930344X.

[54] Horvat, C., Blanchard-Wrigglesworth, E. & Petty, A. Observing waves in sea ice with ICESat-2. *Geophysical Research Letters* (2020). URL https://onlinelibrary.wiley.com/doi/abs/10.1029/2020GL087629.

[55] Kwok, R. Sea ice concentration estimates from satellite passive microwave radiometry and openings from SAR ice motion. *Geophysical Research Letters* **29**, 25–1–25–4 (2002). URL http://doi.wiley.com/10.1029/2002GL014787.

[56] Notz, D., Haumann, F. A., Haak, H., Jungclaus, J. H. & Marotzke, J. Arctic sea-ice evolution as modeled by Max Planck Institute for Meteorology's Earth system model. *Journal of Advances in Modeling Earth Systems* **5**, 173–194 (2013). URL http://dx.doi.org/10.1002/jame.20016 http://doi.wiley.com/10.1002/jame.20016.

[57] Kern, S., Lavergne, T., Notz, D., Pedersen, L. T. & Tonboe, R. Satellite passive microwave sea-ice concentration data set inter-comparison for Arctic summer conditions. *The Cryosphere* **14**, 2469–2493 (2020). URL https://tc.copernicus.org/articles/14/2469/2020/.

[58] Tsujino, H. *et al.* JRA-55 based surface dataset for driving ocean–sea-ice models (JRA55-do). *Ocean Modelling* **130**, 79–139 (2018). URL https://linkinghub.elsevier.com/retrieve/pii/S146350031830235X.

[59] Smith, W. O. & Nelson, D. M. Importance of Ice Edge Phytoplankton Production in the Southern Ocean. *BioScience* **36**, 251–257 (1986). URL https://academic.oup.com/bioscience/article-lookup/doi/10.2307/1310215.

[60] Perrette, M., Yool, A., Quartly, G. D. & Popova, E. E. Near-ubiquity of ice-edge blooms in the Arctic. *Biogeosciences* **8**, 515–524 (2011).

[61] Strong, C. & Rigor, I. G. Arctic marginal ice zone trending wider in summer and narrower in winter. *Geophysical Research Letters* **40**, 4864–4868 (2013). URL http://doi.wiley.com/10.1002/grl.50928.

[62] Letelier, R. M., Karl, D. M., Abbott, M. R. & Bidigare, R. R. Light driven seasonal patterns of chlorophyll and nitrate in the lower euphotic zone of the North Pacific Subtropical Gyre. *Limnology and Oceanography* **49**, 508–519 (2004).

[63] Boss, E. & Behrenfeld, M. In situ evaluation of the initiation of the North Atlantic phytoplankton bloom. *Geophysical Research Letters* **37**, 1–5 (2010).

[64] Matthes, L. C. *et al.* Average cosine coefficient and spectral distribution of the light field under sea ice: Implications for primary production. *Elementa* **7** (2019).

[65] Yu, X., Wu, Z., Jiang, W. & Guo, X. Predicting daily photosynthetically active radiation from global solar radiation in the Contiguous United States. *Energy Conversion and Management* **89**, 71–82 (2015). URL https://linkinghub.elsevier.com/retrieve/pii/S0196890414008395.

[66] Taylor, J. R. & Ferrari, R. Shutdown of turbulent convection as a new criterion for the onset of spring phytoplankton blooms. *Limnology and Oceanography* **56**, 2293–2307 (2011).

[67] Holland, M. M. An improved single-column model representation of ocean mixing associated with summertime leads: Results from a SHEBA case study. *Journal of Geophysical Research* **108**, 3107 (2003). URL http://doi.wiley.com/10.1029/2002JC001557.

[68] Horvat, C., Tziperman, E. & Campin, J.-M. Interaction of sea ice floe size, ocean eddies, and sea ice melting. *Geophysical Research Letters* **43**, 8083–8090 (2016). URL http://doi.wiley.com/10.1002/2016GL069742.

[69] Pellichero, V., Sallée, J.-B., Schmidtko, S., Roquet, F. & Charrassin, J.-B. The ocean mixed layer under Southern Ocean sea-ice: Seasonal cycle and forc-

ing. *Journal of Geophysical Research: Oceans* **122**, 1608–1633 (2017). URL http://doi.wiley.com/10.1002/2016JC011970.

[70] Pinkerton, M. H., Bradford-Grieve, J. M. & Hanchet, S. M. A balanced model of the food web of the Ross Sea, Antarctica. *CCAMLR Science* **17**, 1–31 (2010).

[71] Horvat, C., Seabrook, S., Cristi, A., Matthes, L. & Bisson, K. Code for: The Case for Phytoplankton Blooms Under Antarctic Sea Ice (2021).

7 Corresponding Author

All correspondence and requests for material should be addressed to Christopher Horvat, christopher_horva

8 Acknowledgements

CH was supported by NASA grant 80NSSC20K0959 and in part by Schmidt Futures – a philanthropic initiative that seeks to improve societal outcomes through the development of emerging science and technologies. CH thanks the National Institute of Water and Atmospheric Research in Wellington, NZ for their hospitality during parts of this work. KB was supported by NASA grant 80NSSC20K0970. We acknowledge the World Climate Research Programme, which, through its Working Group on Coupled Modelling, coordinated and promoted CMIP6. We thank the climate modeling groups for producing and making available their model output, the Earth System Grid Federation (ESGF) for archiving the data and providing access, and the multiple funding agencies who support CMIP6 and ESGF.

9 Author Contributions

CH and SS concieved of the study. CH performed the data analysis and prepared the manuscript. KB provided BGC-Argo data processing and analysis. All authors assisted with study design

and manuscript writing.

10 Competing Interests

The authors declare no competing interests.

11 Data Availability

ICESat-2 data are available through the National Snow and Ice Data Center (NSIDC). The sea ice type product is found online at https://nsidc.org/data/ATL07/versions/3. JRA55-do and CMIP6 data used in this study are available at the Earth System Federated Grid at `https://esgf-node.lln` and `https://esgf-node.llnl.gov/projects/cmip6/`, respectively. Argo data were collected and made freely available by the Southern Ocean Carbon and Climate Observations and Modeling (SOCCOM) Project funded by the National Science Foundation, Division of Polar Programs (NSF PLR -1425989 and OPP-1936222), supplemented by NASA, and by the International Argo Program and the NOAA programs that contribute to it. `http://www.argo.ucsd.edu, https://soccompu.princeton.edu/www/index.html`. The Argo Program is part of the Global Ocean Observing System. Processed Argo data for making figures is included in the code repository [71].

12 Code Availability

Code for processing data and producing Antarctic under-ice light fields and UIB-permitting criteria is publicly available on github at https://github.com/chhorvat/Antarctic-Light/, with releases archived in the Zenodo repository [71]. Data required to produce figures in this manuscript is included within this repository.

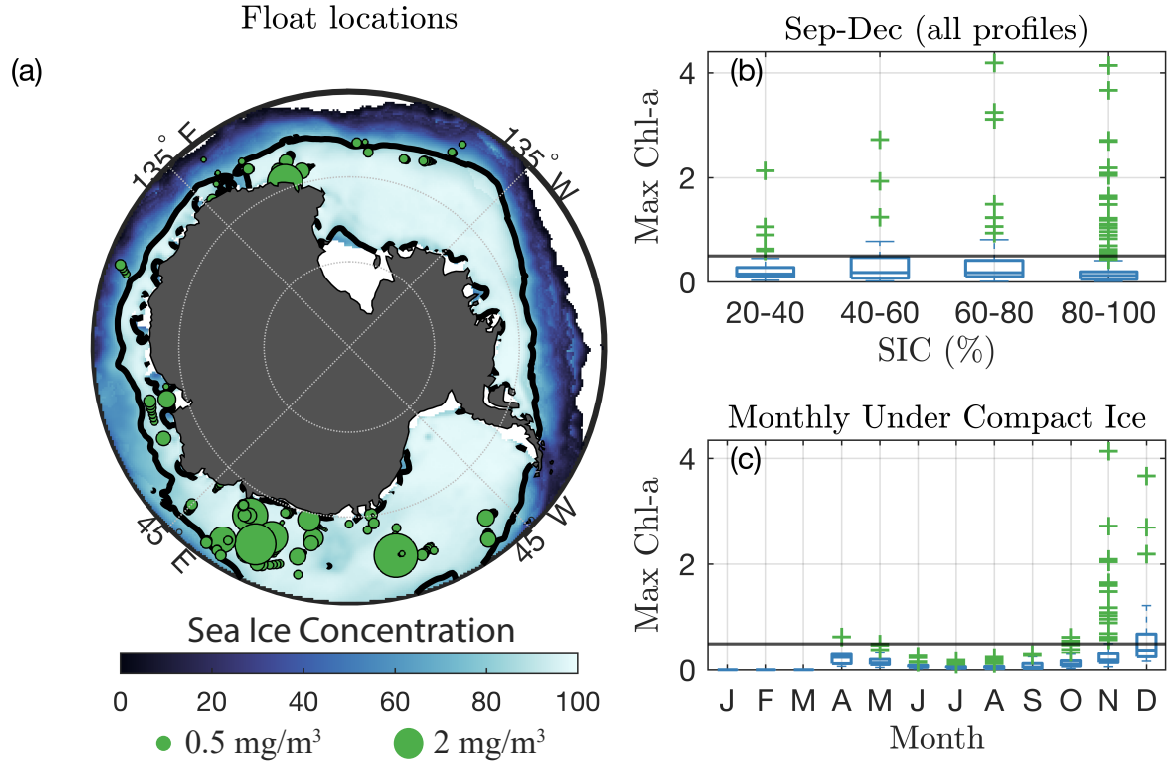

Figure 1: **Chlorophyll-a recorded under compact sea ice by BGC-Argo floats.** (a) Climatological sea ice coverage in September-November, 2014-2020. Black line shows 80% concentration contour. Green circles are locations of under-ice Argo float profiles under compact sea ice from September-December, with sizes scaled with value of Chl_{max}. Green dots outside of map shows sizes corresponding to 0.5 and 2.0 mg/m^3. (b) Box plot of Chl_{max} for all BGC-Argo measurements under sea ice, indexed by sea ice concentration. Whiskers extend boxes ± 3 standard deviations from the mean in each month and vertical blue line is ensemble median. Crosses are outlier values ($\sigma > 3$). Black line is 0.5 mg Chl-a/m^3. (c) Same as (b), but for Chl_{max} recorded under compact sea ice (concentration $> 80\%$) only, indexed by month.

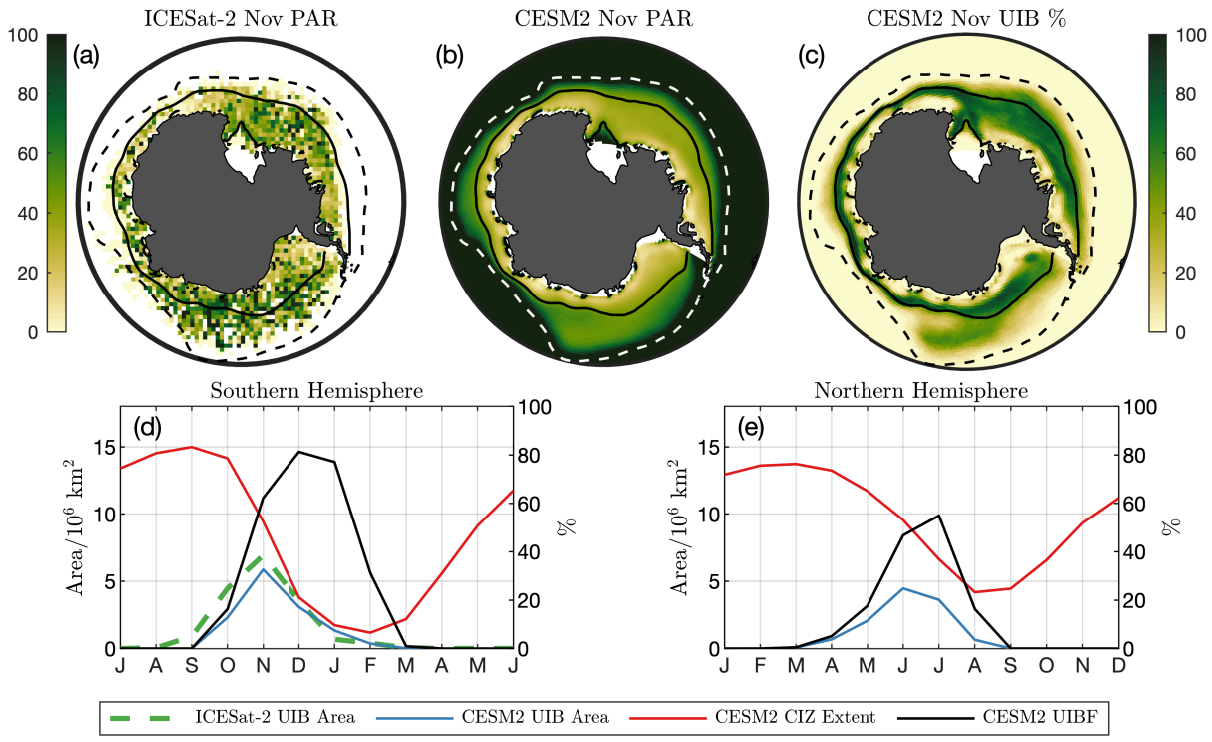

Figure 2: **Light field and UIB potential under Southern Ocean sea ice** (a) 2018-2020 November surface PAR (μmol photons/m^2/s) estimate from ICESat-2. (b) CESM2 climatological PAR from pre-industrial simulation. Solid lines in (a-b) are CESM2 climatological CIZ (concentration above 80%). Dashed lines are climatological SIE (concentration above 15%). (c) CESM2 November UIB%. (d,left axis) Seasonal cycle of CESM2 (red) CIZ extent and (blue) UIB extent. Dashed green line is UIB area from ICESat-2. (d,right axis) CESM2 UIBF. (e) As in (d), but for the Northern Hemisphere. Axes in (d) and (e) are offset by 6 months.

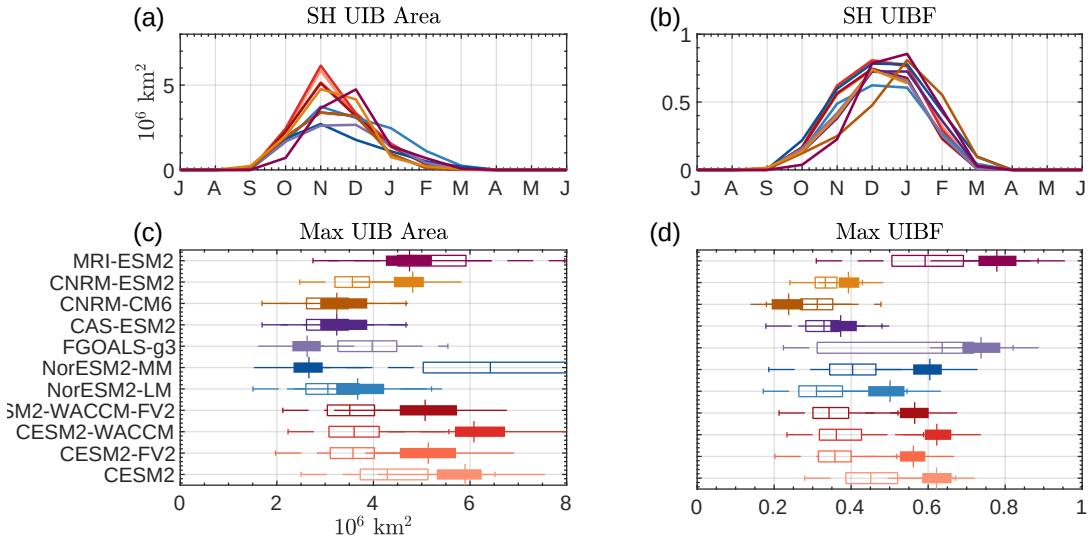

Figure 3: **Statistics of bloom-permitting area for CMIP6 models**. (a) Seasonal cycle of UIB-permitting area in the Southern Hemisphere. (b) Seasonal cycle of UIBF. (c) Box plots of maximum annual UIB area in (filled) the Southern Hemisphere or (unfilled) the Northern Hemisphere. (d) Box plots of UIBF during month of maximum UIB area. Colors of lines in (a,b) correspond to boxes in (c,d)

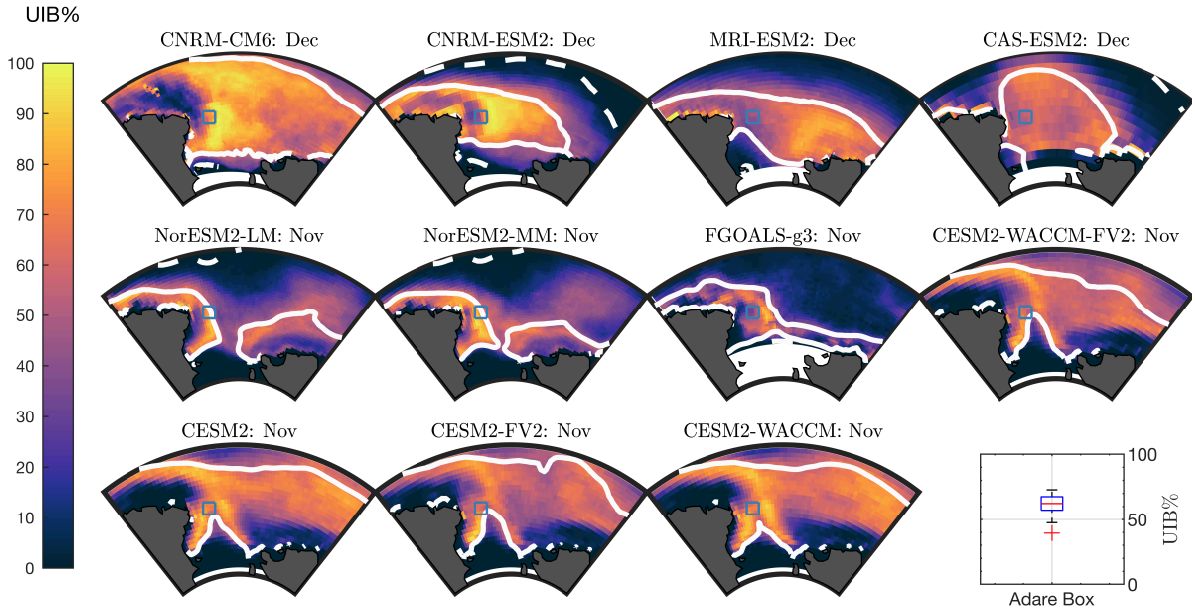

Figure 4: **UIB likelihoods in the Ross Sea.** Ross Sea UIB% for each model in the month of maximum UIB area. Solid lines are climatological CIZ. Dashed lines are climatological SIE. Blue square highlights location of interest at 72°S,178°E. Box plot (bottom right) is of UIB% at square location.